Dental OCT

74

Petra Wilder-Smith, Linda Otis, Jun Zhang, and Zhongping Chen

Keywords
Dental OCT • Oral • Dentistry • Dentin • Enamel • Pulp • Gingival tissue • Tooth decay • Caries • Erosion • Oral mucosa

The oral cavity is a diverse environment that includes oral mucosa, gingival tissues, teeth, and their supporting structures. Oral health is currently evaluated through three main avenues: visual/tactile examination, periodontal probing, and radiographic imaging. After the surfaces are dried with a gentle stream of air, visual examination of the teeth and surrounding soft tissue is completed. Clinicians tactically explore the surface hardness of teeth to detect dental caries while demineralization of the enamel and soft tissue inflammation are characterized by changes in visual characteristics. Probes are also placed between the soft tissue and tooth to assess periodontal health. Radiographs are used to determine the internal structural integrity of the teeth and alveolar bone. Although radiographs are highly sensitive for detecting regions of carious

P. Wilder-Smith
Beckman Laser Institute, University of California Irvine, Irvine, CA, USA
e-mail: pwsmith@uci.edu

L. Otis
Oncology and Diagnostic Sciences, University of Maryland School of Dentistry, Baltimore, MD, USA

J. Zhang
Department of Biomedical Engineering, The Beckman Laser Institute, University of California Irvine, Irvine, CA, USA

Z. Chen (✉)
The Edwards Life Sciences Center for Advanced Cardiovascular Technology, Beckman Laser Institute, Irvine, CA, USA

Department of Biomedical Engineering, The Beckman Laser Institute, University of California Irvine, Irvine, CA, USA
e-mail: z2chen@uci.edu

W. Drexler, J.G. Fujimoto (eds.), *Optical Coherence Tomography*,
DOI 10.1007/978-3-319-06419-2_76

demineralization and alveolar bone loss, they have several limitations. Since radiographs are two dimensional, precisely locating the position of a carious lesion or osseous defect is impossible. Radiographs cannot distinguish active from inactive disease and cannot identify periodontal disease until after bone loss has occurred. Finally, radiography uses harmful ionizing radiation and provides no information on soft tissue status.

Optical coherence tomography (OCT), a well-known technique for creating noninvasive, high-resolution (<20 μm) images of biological microstructure, has been used in dentistry. In vitro images of porcine dental tissues were first reported in 1998 [1]; subsequently in vivo imaging of human dental tissue proved that OCT could be used as a valuable diagnostic aid for several applications within dental medicine [2, 3]. The goal of dental OCT is to produce in vivo images of oral microstructure that can be used to make qualitative and quantitative assessments of oral tissues. In particular, OCT images depict at high resolution clinically important anatomical features such as the location of the soft tissue attachment, morphological changes in gingival tissue, tooth decay, enamel thickness and decay as well as structural integrity of dental restorations. Because OCT images both the hard and soft tissue structures of the oral cavity at high resolution, it offers the unique capacity to identify dental disease before destructive changes have progressed allowing for earlier intervention than is possible with current diagnostic modalities.

The oral cavity begins at the lips and ends posteriorly at the area of the palatine tonsils. This chapter will focus on the following structures within the oral cavity:

1. The hard dental tissues, i.e., the teeth.
2. The periodontal tissues, i.e., the supporting tissues for the teeth. These include soft tissues, as well as cementum, periodontal ligament, and bone.
3. The oral mucosa, i.e., the lining of the oral cavity.

This section will address all the anatomical structures within the oral cavity that are listed above. A brief review of normal oral structures will be followed by a summary of the pathologies affecting each structure, a discussion of existing diagnostic tools, and an overview of diagnostic usage of OCT in each structure to date. In the final section, the authors present their views on the potential use of OCT in dentistry in the future.

74.1 Hard Dental Tissues

74.1.1 Definition of Dental Hard Tissues

The tooth consists of enamel, dentin, and pulp (Fig. 74.1). The close relationship that exists during the formation of these three tissues is maintained in the structure of the tooth.

74.1.1.1 Enamel

Consisting of 95 % mineral, 1 % water, and 4 % organic material by weight [4], enamel is the hardest structure of the body. The inorganic content of enamel consists of a crystalline calcium phosphate known as hydroxyapatite, which is also found in bone, calcified cartilage, dentin, and cementum. Although the vast

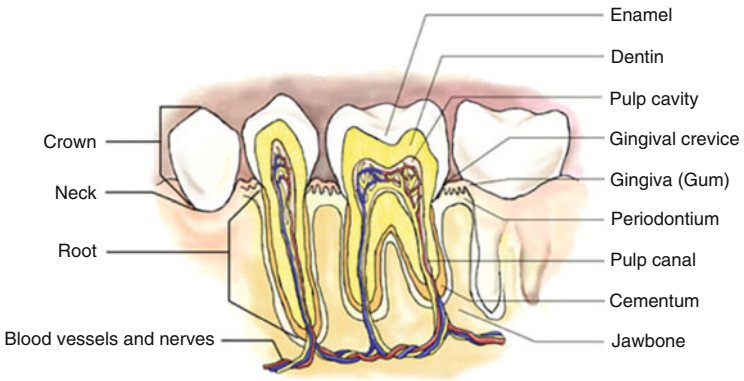

Fig. 74.1 Structure of tooth and periodontium (DeEtte M. DeVille, M.D. AMA atlas of the body: the teeth © Copyright 1999 American Medical Association)

majority of the enamel is occupied by densely packed hydroxyapatite crystals, a fine lacy network of organic material appears between the crystals. The bulk of this organic material is made up of the TRAP (tyrosine-rich amelogenin protein) peptide sequence tightly bound to the hydroxyapatite crystal as well as nonamelogenin proteins [4].

Because of its high mineral content, enamel is extremely hard and brittle. Ground sections of enamel reveal roughly rodlike cylindrical structures 4–6 um in diameter within the enamel, which owe their existence to a highly organized pattern of hydroxyapatite crystal orientation. For the most part, the long axes of the crystals run parallel to the longitudinal axis of the rod. This is particularly true for crystals along the central axis of the rod. Crystals more distant from the central axis, however, flare laterally to an increasing degree as they approach the rod periphery. The interrod region is an area surrounding each rod in which crystals are oriented in a different direction from those constituting the rod [4]. The capacity of OCT to image the orientation of the enamel rods and interrod region is illustrated in Fig. 74.2.

The enamel surface varies with age. In unerupted teeth, it consists of a structureless cuticle 0.5–1.5-um thick [4] overlying a 5-nm thick layer of small loosely packed crystallites interspersed with a few large platelike crystals and cuticular material [4]. This layer merges into the subsurface enamel, where 50-nm crystals are loosely packed. The subsurface layer forms the enamel surface due to rapid loss of the primary cuticle and the surface layer of small crystallites soon after eruption. An organic deposit called the salivary pellicle is present on the tooth surface, usually covered by a layer of dental plaque [4]. The important role of dental plaque in fostering dental decay will be discussed below.

74.1.1.2 Dentin-Pulp Complex

The dentin supports the enamel. The junction between the two tissues is a series of scallops where crystals of enamel and dentin intermix. Dentin and pulp are embryologically, histologically, and functionally the same tissue and are therefore

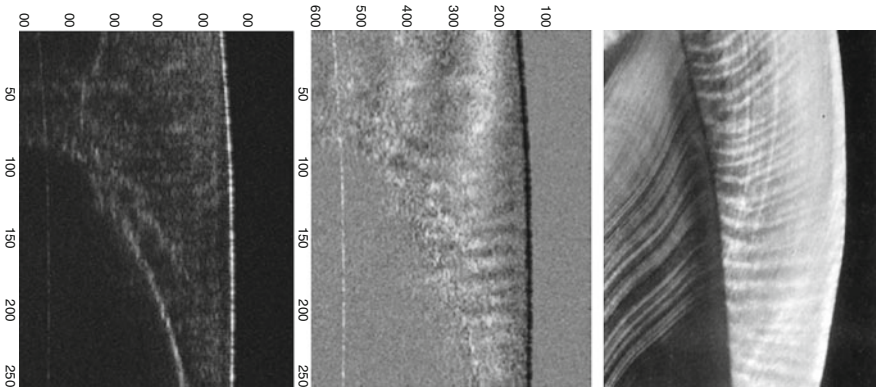

Fig. 74.2 Conventional and polarization-sensitive OCT images and a ground section of a human tooth reveal the superior capacity of polarization-sensitive OCT to image the orientation of the enamel rods and the interrod region. The junction between the enamel and dentin is characterized by a series of scallops where dentin and enamel intermix [6]

considered together here [5]. Mature dentin is, chemically, by weight, approximately 70 % inorganic material, 20 % organic material, and 10 % water (adsorbed onto the surface of the mineral or in interstices between crystals). The main inorganic component is hydroxyapatite; the main organic phase is type 1 collagen with fractional inclusions of glycoproteins, proteoglycans, phosphoproteins, and some plasma proteins. Approximately 56 % of the mineral phase is within the collagen. Due to its inorganic phase, dentin is slightly harder than bone and softer than enamel [5]. Physically, dentin has an elastic quality; it is bound to the enamel at the dentinoenamel junction and covered by cementum in the root of the tooth [5].

Forming the bulk of the tooth, dentin consists of multiple closely packed dentinal tubules traversing its entire thickness and containing the cytoplasmic extensions of odontoblasts that once formed the dentin and now maintain it. The cell bodies of these odontoblasts lie along the inner aspect of the dentin, where they also form the peripheral boundary of the dental pulp [5]. The dental pulp is the soft connective tissue occupying the pulp space in the central area of the tooth, which is divided into the coronal (upper) portion, the pulp chamber, and the lower portion, the root canal. The root canals end at the apical foramen, where the main blood vessels and nerves to the pulp enter and leave the tooth. Through the apical foramen, pathologies can migrate between the pulp and the periodontium [5].

Three types of dentin are recognized in human teeth [5]. The bulk of the tooth consists of primary dentin. The structurally somewhat less regular secondary dentin develops after root formation is complete. Tertiary dentin is produced in reaction to noxious stimuli such as decay or dental procedures and is very heterogeneous in its structure. Viewed microscopically, dentin consists of several structural features. Dentinal tubules are tapered structures approximately 2.5 um in diameter near the pulp, narrowing down to approximately 900 um near the dentinoenamel junction [5]. They extend through the entire thickness of the dentin from the

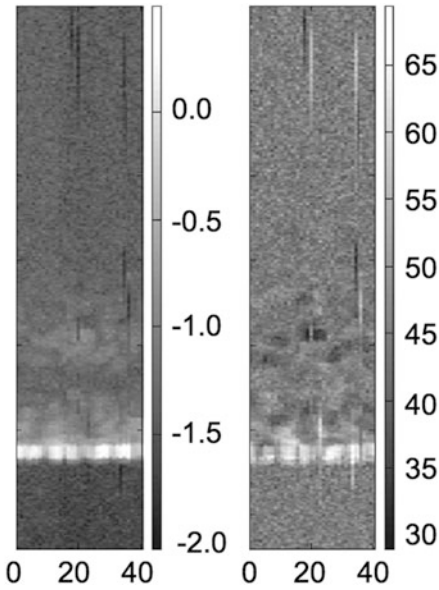

Fig. 74.3 OCT images of a human tooth near the DEJ reveal irregular masses of decreased signal intensity that were 10–20 μm in diameter and consistent with the morphology of interglobular dentin that can be seen in conventional and PS-OCT [6]

dentinoenamel junction to the pulp, following an S-shaped path. At their pulpal end, the tubules are generally thought to contain the process of an odontoblast bathed in dentinal fluid, although there is some uncertainty regarding the exact nature of tubule content [5]. The tubular structure of dentin permits the rapid progression of pathologies and accentuates the pulpal response to dentinal events [5]. It also allows for excellent light propagation into the pulp.

Within the dentinal tubule exits a hypermineralized (40 % more than regular dentin) ring of intratubular dentin causing a progressive reduction and the potential for eventual obliteration of the lumen of the tubule [5]. Exact mechanisms and causes are still uncertain. Intertubular dentin is located between the dentinal tubules and consists of a tightly woven network of type 1 collagen fibrils arranged roughly at right angles to the dentinal tubules, with apatite crystals deposited between and parallel to the fibrils. The ground substance consists of phosphoproteins, proteoglycans, and γ-carboxyglutamate [5]. Interglobular dentin consists of areas of unmineralized or hypomineralized dentin where zones of mineralization have failed to fuse. Here the normal architectural pattern of the tubules remains unchanged, except for the lack of intratubular dentin. The intraglobular dentin can be visualized in PS-OCT images of dentin (Fig. 74.3).

The dental pulp is the soft connective tissue that supports the dentin. Principal cells within the pulp include odontoblasts, undifferentiated mesenchymal cells, fibroblasts, macrophages, and other immunocompetent cells [5]. The major vessels and nerves lie in the central portion of the pulp. The principal collagen fibers of the pulp are type l and type lll collagen [5] in a glycosaminoglycan-, glycoprotein-, and water-containing ground substance.

74.1.2 OCT Imaging of the Hard Dental Tissues

Marked light scattering limits the transmission of visible light at 400–700-nm wavelengths through tooth substance. The relationship between light scattering in enamel and wavelength (λ) is defined as $1/\lambda^3$. At longer wavelengths exceeding 1,500 nm, light absorption by water becomes a limiting factor for the absorption of infrared (IR) light [6–8] Therefore, OCT imaging of the tooth is best performed at wavelengths between 700 and 1,500 nm, with excellent penetration to a depth of 1.5–3 mm. In 2000, Otis et al. demonstrated the superior imaging and penetration of OCT systems using a 1,310-nm vs. 850-nm light source [9].

In 1998, Colston et al. presented the first in vivo optical coherence tomography (OCT) images of dental tissue [1]. The authors presented a dental optical coherence tomography system with a very promising feature – the incorporation of the interferometer sample arm and transverse scanning optics into a handpiece suitable for intraoral use. Examples of use of this imaging system for dentistry illustrated its potential for diagnosis of periodontal disease, detection of caries, and evaluation of dental restorations. The average imaging depth of this system varied from 3 mm in hard tissues to 1.5 mm in soft tissues. Axial resolution was 15 μm (free space). The system had a lateral resolution of 50 μm and an average total lateral scan distance of 12 mm. The total scan time for each image was approximately 45 s. Further studies by this and other groups have clearly demonstrated the effectiveness of OCT for rapid, high-resolution imaging of dental tissues using OCT (please see the appropriate sections below).

Active work in the area of OCT probe development has greatly enhanced the applicability of OCT imaging for dental applications [10–20]. Figure 74.4 shows the schematic diagram and picture of a miniature probe based on a dual axis microelectromechanical system (MEMS) mirror [11]. The MEMS mirror provides high-speed, 2-axis scanning while occupying a very small volume with extremely low power consumption. The dimensions of the MEMS mirror in Fig. 74.4b are 800-mm diameter, and both axes are capable of scanning up to 30° angles at frequencies greater than 3 kHz with good linearity. The packaged probe with an outer diameter 5.0 mm or smaller can be assembled, which is sufficiently compact for dental applications (Fig. 74.4c).

The 2D MEMS probe shown in Fig. 74.4c has been used for in vivo imaging of animal models and human subjects. The representative in vivo 3D images from rabbit and human tissues are shown in Fig. 74.5. These images were acquired employing the FD-OCT system, which provides adequate imaging speed for 3D imaging.

In addition to side-viewing probes based on MEMS, forward-viewing probes based on cantilever-type scanning have been demonstrated by several groups [19–24]. The scanning probes are driven by either PZT, electrostatic, or magnetic force [19–24]. Recently, a forward-view OCT scanning probe based on a fiber-cantilever piezotube scanner was developed by using a semi-resonant scan strategy for a better scan performance (Fig. 74.6a) [20]. A cantilever weight was attached to the fiber cantilever to reduce the resonance frequency down to 63 Hz, well in the desirable range for FD-OCT. By driving the two axes at slightly different

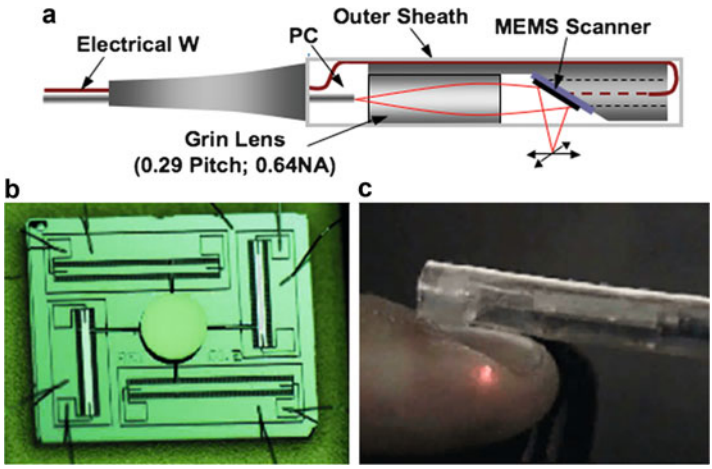

Fig. 74.4 (**a**) Schematic diagram of endoscopic probe; (**b**) photo of a vertical 2-D scanning MEMS based on comb-drive actuator. (**c**) photo of assembled 2-D miniature probe [11]

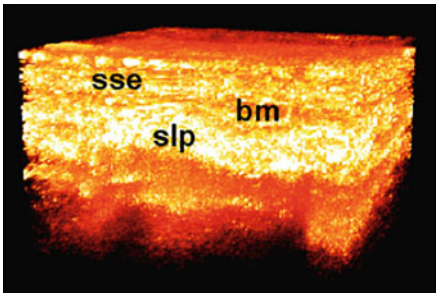

Fig. 74.5 In vivo 3D imaging of true human vocal cord obtained by a FD-OCT system using the 2D MEMS probe. Image size is 1 × 1 × 1.4 mm. Important structures, such as the stratified squamous epithelium (*sse*), basement membrane (*bm*), and superficial lamina propria (*slp*), are clearly visible

frequencies, a low-order Lissajous pattern was obtained for a 2D area scan (Fig. 74.6b). 3D OCT images were successfully acquired in an acquisition time of 1.56 s for a tomogram volume of 2.2 × 2.2 × 2.1 mm^3 (Fig. 74.6c).

These studies demonstrate the capabilities of a miniature probe for 3D OCT imaging. A 3D OCT system employing a high-speed, compact scanner may have the potential to expand the applications of OCT for dental and oral imaging and may revolutionize areas of clinical medicine as well as medical research.

74.1.3 Pathologies of Hard Dental Tissues

74.1.3.1 Decay

The most common pathological condition of the tooth is decay or caries. Cause is a confluence of cariogenic diet and inadequate oral hygiene on a susceptible tooth

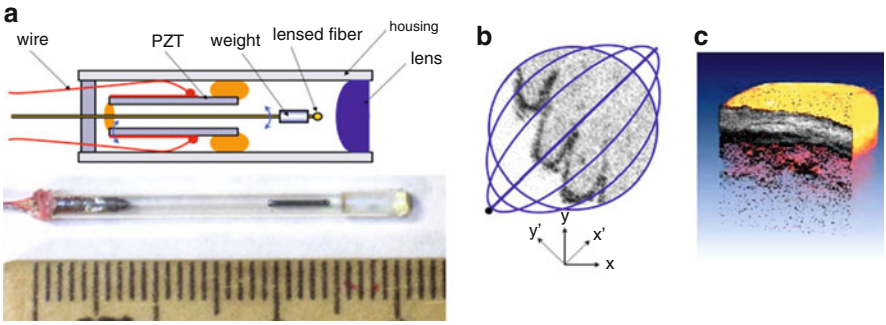

Fig. 74.6 (**a**) Schematic design and picture of the fabricated OCT scanning catheter. The dimensions are given in millimeters; (**b**) schematic Lissajous scan pattern (*blue lines*) in the XY plane laid over an OCT *en face* image; (**c**) the 3D-rendered tomogram [20]

surface. Microorganisms multiply at the tooth surface, forming a layer of plaque. These microorganisms produce lactic and acetic acid, reducing the pH to levels as low as 3.5. At lower pHs, hydroxyapatite becomes increasingly soluble, leading to rapid demineralization and increased porosity and permeability as the calcium bound to the hydroxyapatite is ionized and washed out by the saliva. Decayed or carious lesions usually are associated with a darkening in color. However, some carious enamel lesions appear bright at the surface, especially in their early stages and are thus difficult to detect [25]. An important characteristic of the early carious lesion is that most of the demineralization occurs at the subsurface level, so that a well-mineralized surface zone remains in place for some time. This has an important implication for the early detection of carious lesions, namely, the inability to detect early lesions by clinical visual inspection of the tooth surface alone.

Diagnostic confidence also has significant impact on whether the clinician chooses to initiate further preventive therapy or restorative intervention. When caries reach the dentin, the response is sequential. Frequently at this stage, the enamel is physically still grossly intact, and bacterial invasion has not occurred. However, the lesion has increased the permeability of enamel to acid and other chemical stimuli, which now evoke a response from the dentin-pulp complex such as the deposition of tertiary dentin. Once the enamel cavitates, bacteria reach the dentin surface, and destruction of dentin begins [26].

Current Methods for Diagnosis of Caries

The technologies currently available to dental clinicians for the detection of dental caries have limited sensitivity, and there is controversy surrounding the "gold standard" for caries diagnosis. Detection of pit and fissure caries by all current methods is low. While radiographs reveal approximal lesions with moderate sensitivity and high specificity, occlusal caries are grossly underestimated in radiographic examinations [27–29]. Moreover, the widespread use of fluorides has increased the diagnostic difficulty of pit and fissure caries because enamel remineralization conceals dentinal lesions that continue to progress [29, 30].

Recently, tactile examination with a sharp explorer has been discouraged, since this may produce breakdown of the enamel surface or transfer cariogenic organisms to unaffected sites. Moreover, probing does not increase diagnostic accuracy as compared with visual examination alone [31]. Thus, visual diagnosis has been suggested as the diagnostic method of choice for pit and fissure caries [32, 33]. Trained observers detect small pit and fissure lesions by visual examination with a sensitivity of 0.6 and a specificity of 0.8. This means that 40 % of true dentinal lesions are classified as sound and that 15 % of sound surfaces are classified as diseased. In populations with a low prevalence of caries, the disease usually progresses slowly. Thus, in low prevalence caries populations, traditional diagnostic techniques worked because it is better to err toward false-negative diagnoses than to restore a sound tooth. Limited sensitivity worked in classical operative approaches, because teeth were not restored until caries involvement was significant and then the restoration was extended to include all tooth structure in the vicinity that would be considered "susceptible to caries." Current therapies first employ preventive strategies when lesions are small and the caries risk is low. When the tooth surface is cavitated, caries significantly involve the dentin, or when caries risk is high, the diseased dentin is removed with minimal surrounding tooth structure. For today's dentistry, the sensitivity of traditional diagnostic methods is unacceptable. The materials and operative technology permit placement of small restorations with removal of only the diseased dentin and a minimal amount of sound tooth structure. The success of these minimally invasive operative approaches depends on locating the precise region of active caries and determining with certainty that the remaining tooth structure is caries free [33]. A more precise caries diagnostic method would greatly improve the current standard of dental preventive and restorative care, with a major impact on dental health care delivery [34].

Dentists continue to rely primarily on visual and tactile examination, supported by radiographic data. However, early detection of demineralization and quantification of tooth substance loss using these techniques is extremely difficult, so that dental erosions are usually diagnosed at a relatively advanced stage when substantial irreversible enamel loss has occurred.

OCT Diagnosis of Caries

Studies indicate that OCT is a powerful technique for detecting subsurface changes in the material properties of dental tissues. OCT reliably identifies changes in dentin under sealants and adjacent to the margins of composite restorations. Comparing OCT profiles over time should allow clinicians to quickly detect potential sites of disease progression or monitor the results of remineralization therapy. Most groups have taken one of two approaches to use OCT for the detection and assessment of dental caries, using either conventional time-domain OCT or polarization-sensitive OCT.

Conventional Time-Domain OCT

Amaechi et al. [35] described the quantitative assessment of dental caries using A-scans (depth versus reflectivity curve), B-scans (longitudinal images), and C-scans (transverse images at constant depth). While the B- and C-scans

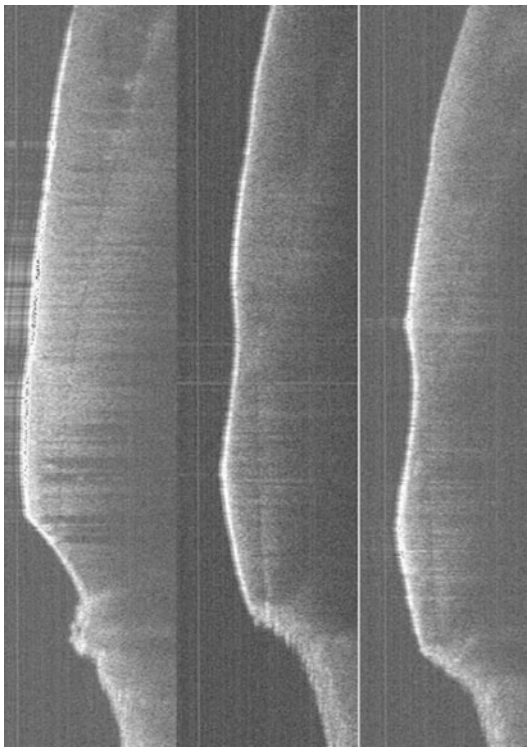

Fig. 74.7 The three OCT images show baseline enamel thickness following two five-minute exposures to a cola beverage (Otis unpublished data)

qualitatively described the lesion detected, the A-scan which showed the depth-resolved reflectivity (dB) of the tooth tissue was used for the quantitative analysis. The percentage reflectivity loss ($R_{\%}$) in demineralized tissue, which related to the amount of mineral loss, increased with greater demineralization time. It was concluded that, using this approach, OCT could quantitatively monitor the mineral changes in a caries lesion on a longitudinal basis. In a later paper, the same group confirmed this correlation using QLF (quantitative light-induced fluorescence) [36].

A novel approach by Ko et al. combined optical coherence tomography (OCT) and Raman spectroscopy to provide morphological information and biochemical specificity for detecting and characterizing incipient carious lesions found in extracted human teeth [37]. OCT imaging of tooth samples demonstrated increased light backscattering intensity at sites of carious lesions as compared to the sound enamel (Fig. 74.7). Using Raman microspectroscopy and fiber-optic-based Raman spectroscopy to characterize the caries further, they demonstrated excellent potential for a new fiber-optic diagnostic tool enabling dentists to identify early caries lesions with greater sensitivity and specificity. In a follow-up study, Sowa et al. compared the caries diagnostic capabilities of the A-scan intensity, the OCT attenuation coefficient as well as the mean and standard deviation of the lognormal fit to the histogram of the A-scan ensemble. The OCT attenuation coefficient showed the highest discriminatory capacity. However, direct analysis of the

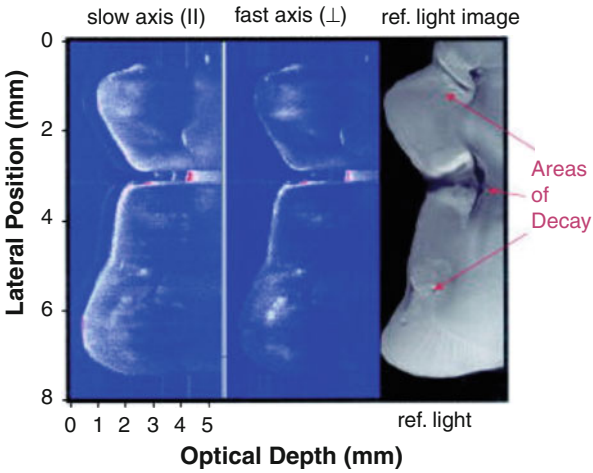

Fig. 74.8 Slow and fast axis OCT scans across the top of a third molar with occlusal decay. The reflected light image of the tooth section is shown on the right for comparison. All three carious areas are resolved in the OCT images with very strong scattering (*red*) in the base of the fissure shown in the *center*. The intensity varies from –40 to 10 dB with intensities of less than –39 dB demarcated in *blue* and those of intensity greater than 5 dB in *red* [43]

A-scans or the histogram of A-scan intensities also showed good diagnostic discrimination [38].

The capability of OCT for early detection and evaluation of root caries was described by Amaechi et al. [39]; its potential for detecting and mapping deficient restorations was also demonstrated by de Mello et al. [40].

Polarization-Sensitive OCT

Birefringence of dentin and enamel provides PS-OCT with a contrast agent useful in indicating pre-carious or carious lesions [31]. PS-OCT can provide additional information related to the mineralization status and/or the scattering properties of the dental materials (Fig. 74.8). Several authors have described the use of PS-OCT for detection and diagnosis of demineralization and dental caries [41–46].

74.1.3.2 Dental Erosion, Attrition, Abrasion, and Cracking

Erosion is defined as the progressive loss of hard dental tissue by chemical processes not involving bacterial action. Repeated or prolonged exposure of teeth to acid leads to selective dissolution of specific components of the tooth surface, with eventual loss of tooth substance, hypersensitivity, caries, functional impairment, and even tooth fracture. The critical pH for enamel dissolution is 5.5. It is estimated up to 80 % of children and over 40 % of adults demonstrate substantial loss of tooth substance, an increasing proportion of which may be related to dental exposure to gastroesophageal reflux disease [47–51]. If enamel demineralization is detected sufficiently early, the enamel can be remineralized before damage becomes irreversible.

Loss by wear of tooth or restoration surface caused by tooth-to-tooth contact during mastication or parafunction is defined as attrition, whereas loss of dental tissue by wear from exogenous substances such as toothbrushes is termed abrasion. Enamel tissue loss is permanent, potentially disfiguring and can be costly and sometimes challenging to repair or mask.

Hairline cracks and fractures in the tooth tend to occur after trauma or excessive loading, especially in older patients. If these remain undetected, they can lead to pain, flawed diagnosis, and inappropriate or failed therapy.

Current Methods for Diagnosis of Dental Erosion, Attrition, Abrasion, and Fracture

The technologies currently available to dentists for the diagnosis of tooth loss include visual inspection and radiography. Diagnosis usually occurs at a relatively advanced stage (1) when substantial enamel loss has occurred, (2) damage is irreversible, and (3) differential etiological diagnosis is very tenuous. Monitoring the effectiveness of remineralizing therapies is not possible with conventional clinical tools. Diagnostic tools for cracks and fractures are limited to visual inspection and probing, neither of which is reliable. Radiographs are seldom useful.

OCT Diagnosis of Dental Erosion, Attrition, Abrasion, and Fracture

Optical coherence tomography (OCT) techniques are well suited to the quantification and imaging of enamel loss [40]. A recent publication described the use of in vivo OCT imaging to determine the effectiveness of a proton pump inhibitor to treat gastroesophageal reflux (GERD) by measuring enamel loss through erosion from OCT images [51]. The study was significant in that researchers were able to identify an association between the medication and a reduced enamel erosion vs. the control (placebo) group after a period of only 4 weeks based on the imaging data (Fig. 74.9). Several studies report on the effectiveness of OCT imaging for detecting tooth fractures and cracks, including hairline cracks in the root surface (Fig. 74.10). OCT imaging gave results compatible to far more expensive micro-CT that uses ionizing radiation. Visual observation was relatively ineffective [52, 53].

74.1.4 Caries Prevention: Fluorides and Sealants

The most common methods of caries prevention include systemic fluoride ingestion during tooth development, topical fluoride application, especially during and directly after tooth eruption, and the use of dental sealants. Typically, sealants are placed over vulnerable areas of the teeth, especially the fissures of erupting permanent teeth, to protect them from demineralization and decay during their first few years in the oral cavity, when they are most vulnerable to demineralization and decay. Early detection of decay under sealants is important to avoid major spread of decay underneath the protective covering.

74.1.5 Diagnosing Sealant and Restoration Integrity

Radiographic evaluation and clinical examinations such as visualization and tactile probing of restoration margins are the less than adequate modalities currently available to clinicians. The capacity of OCT to image dental composite restorations

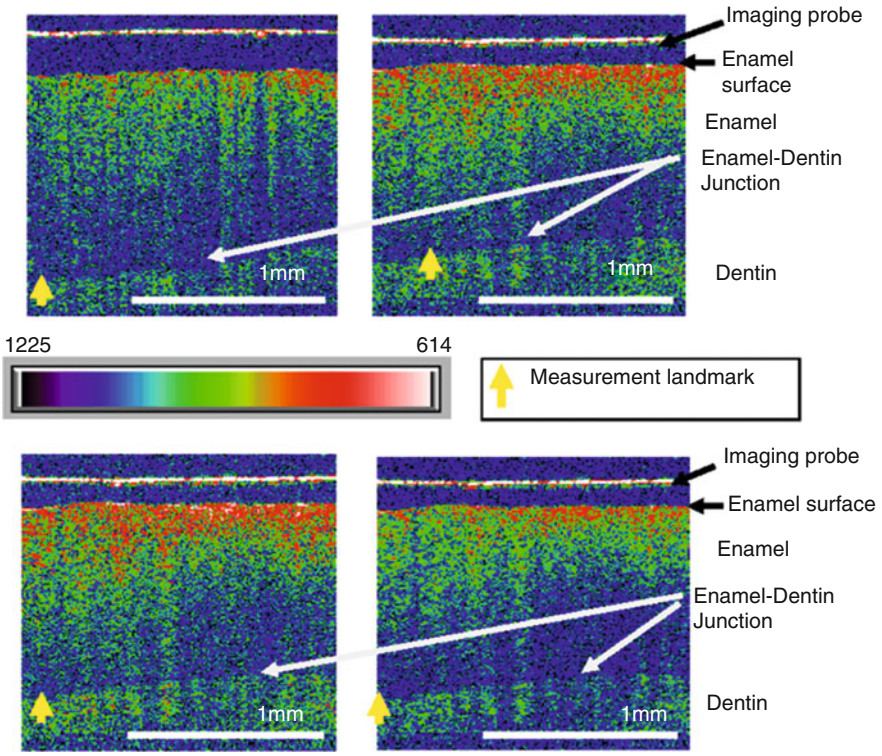

Fig. 74.9 *Above*: In vivo OCT images with pseudo-color superimposition of the same tooth before and after 3-week treatment with placebo. The optical signal near the tooth surface has increased as shown by the greater preponderance of *green* versus *blue*. *Below*: In vivo OCT images with pseudo-color superimposition of the same tooth before and after 3-week treatment with esomeprazole 20 mg bid. The optical signal near the tooth surface has decreased as shown by the reduced preponderance of *red* versus *green* [51]

offers a superior assessment as compared to radiographic imaging [54, 55]. In one study the internal characteristics of facial composite restoration were distinguished, and variations in cavosurface margins accurately identified teeth in restorations with axial cavity depths of 1, 2, and 3 mm. When the teeth were subsequently sectioned, photomicrographs revealed that OCT images depicted with fidelity the composite restorations, dentin-enamel junction (DEJ), and external tooth contours. Minimal spatial distortion of the axial wall was noted in the restorations with axial depths of 1 and 2 mm [56].

OCT has also been shown to identify accurately occlusal sealants and composite restorations [57]. In one study, 21 dentists were asked to interpret OCT images of 9 premolars that were either not restored, contained an occlusal sealant, or were restored with a composite restoration. Following a brief training period, 21 dentists evaluated the OCT images following a randomized blind protocol. The sensitivity

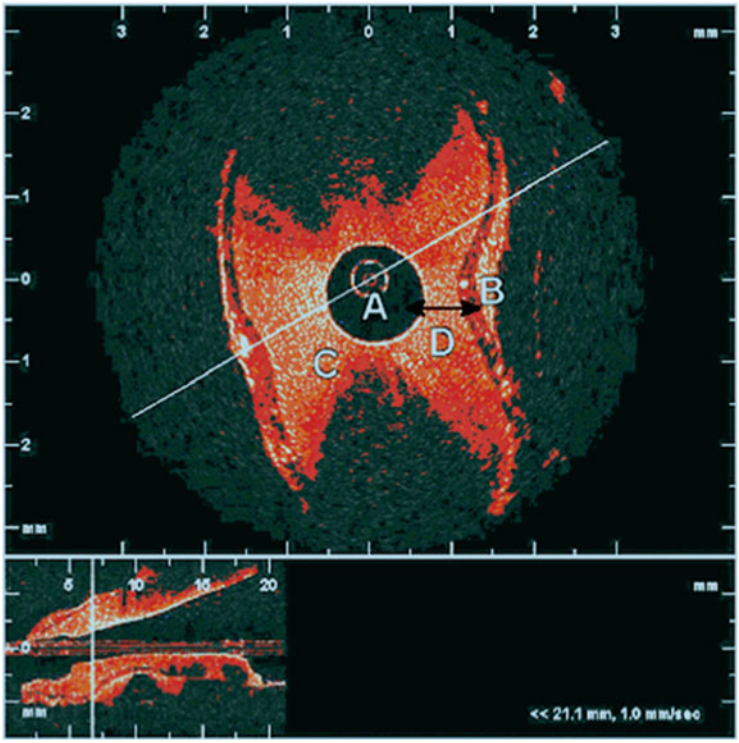

Fig. 74.10 The OCT output at 7 mm from the apex shows a cross-section of a prepared canal. (***A***) The root canal, (***B***) cementum, and (***C***) dentinal tubules. (***D***) "Risk zone" (canal wall 1-mm thick) [52]

of OCT to discriminate composite and sealants was greater than 0.92, while the specificity of discrimination was greater than 0.94. The capacity of OCT to discriminate sealants from non-restored occlusal surfaces was slightly less (sensitivity 0.88; specificity 0.86) but still within a clinically acceptable level. Inter- and intra-rater reliabilities as measured by the kappa statistic also revealed excellent performance by dentists using OCT ($k = 0.82–1.0$). This study also demonstrated that dentists who were previously unfamiliar with OCT images could be trained to interpret the images with a high degree of accuracy.

Not only does OCT detect sealants, it also effectively diagnoses decay underneath sealants. A study by Holtzman et al. evaluating the ability of dentists to detect decay beneath commonly used dental sealants using OCT found that, after 90 min training, dentists were able to detect tooth decay in enamel and under sealants more accurately using OCT than with visual or radiographic examination (Fig. 74.11). Detection using OCT was somewhat better prior to sealant placement than afterward. This effect varied in size depending on the type of sealant used. Radiographic diagnosis was also less accurate after sealant placement. Of the four dental sealants,

Delton provided excellent positive predictive value and the best post-sealant negative predictive values [58].

A paper by Jones et al. described the effective use of polarization-sensitive optical coherence tomography (PS-OCT) to image lesions underneath composite sealants [59]. The polarization-sensitive system, recording images in both the parallel and perpendicular axes, was useful for enhancing the image contrast of the artificial caries and minimizing the interference of the strong reflections at surface interfaces. The artificial lesions could be detected under 750 μm of visibly opaque sealant. Tooth-colored sealants allow deeper imaging depth. The artificial lesions could be detected under 1,000 μm of sealant.

Finally, OCT can be used to assess the internal structure and marginal adaptation of cemented crowns. Cross-sectional images were made in duplicate on the midfacial surface of cemented functional crowns with well-adapted margins and no clinical evidence of recurrent caries. The internal structure and marginal adaptation of porcelain fused to metal crowns were clearly visualized in teeth imaged in vivo. Characteristic image layers that corresponded to incisal and body porcelain were visualized [60].

Using three-dimensional OCT imaging, it is possible to evaluate the structural integrity and wear of composite resin restorations. An OCT contour map of restoration surfaces can be used to quantify volumetric loss or surface changes in a restorative material over time. Wear estimates correlate well with the value as determined by the traditional method of measuring composite wear, the ML scale ($r = 0.86$; $p < 0.05$). OCT images can record changes in the restoration surface that occurred with occlusal function. It was also shown that a region of catastrophic failure not visible clinically or radiographically was detected by OCT [61].

74.2 Periodontal Tissues

Periodontal diseases are a major cause of tooth loss. They are plaque-induced inflammatory disorders that result in the loss of tooth support through the apical migration of connective tissue attachment which results in the resorption of alveolar bone. To establish the diagnosis of periodontitis, it is necessary to detect the loss of connective tissue attachment and alveolar bone [62]. Traditionally, the location of the periodontal attachment has been estimated by mechanically measuring the distance a probe penetrates the soft tissues surrounding the tooth. Attachment level is defined clinically as the distance from a fixed reference point on the tooth (the cementoenamel junction) to the most apical extent of probe penetration. Probing depth is the distance from the gingival margin to the most apical extent of probe penetration. Accurate assessment of probing depth and changes in soft tissue attachment level are critically important in periodontics.

Current methods of periodontal probing use conventional, mechanical, or pressure-sensitive probes. Unfortunately, as a measurement technique, periodontal

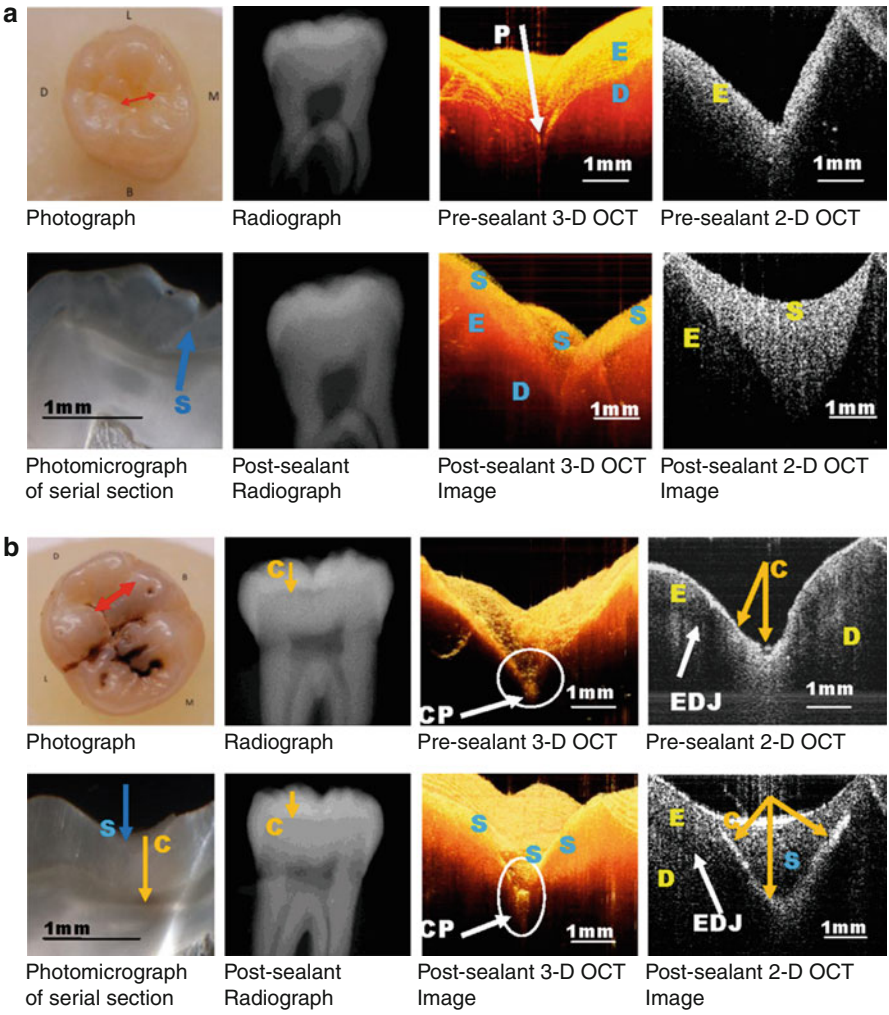

Fig. 74.11 Typical pre- and post-sealant photographic, radiographic, and OCT images as well as photomicrograph of histological section of healthy tooth (**a**) and carious tooth (**b**). (**a**) Images of healthy tooth sample pre- and post-sealant (Fuji TRIAGE sealant) *Above*: LHS: photograph with *red arrow* indicating OCT scan line; *Center left*: pre-sealant radiograph; *Center right*: pre-sealant 3D OCT image; RHS: pre-sealant 2D OCT image. *Below*: LHS: photomicrograph of histological section of tooth, *blue arrow* indicates sealant; *Center left*: post-sealant radiograph; *Center right*: post-sealant 3D OCT image; RHS: post-sealant 2D OCT image. P-occlusal pit; *E* enamel, *D* dentin, *S* sealant. (**b**) Images of decayed tooth sample pre- and post-sealant (Delton sealant) *Above*: LHS: photograph with *red arrow* indicating OCT scan line; *Center left*: pre-sealant radiograph with *yellow arrow* indicating caries (*C*); *Center right*: pre-sealant 3D OCT image with carious occlusal pit (*CP*) indicated by *white arrow*; RHS: pre-sealant 2D OCT image with occlusal caries (*C*) indicated by *yellow arrow* and EDJ indicated by *white arrow*. *Below*: LHS: photomicrograph of histological section of tooth, *blue arrow* indicates sealant (*S*), and *yellow arrow* indicates caries; *Center left*: post-sealant radiograph with *yellow arrow* indicating caries

probing has several sources of error that make it somewhat imprecise [63]. For example, the extent of probe penetration varies with insertion force [64], inflammatory status of the tissues [65], and diameter of the probe tip [66, 67]. Therefore, under routine clinical conditions, periodontal probes have an average measurement error of approximately ± 1 mm [68]. Examiner variation is a major source of error for conventional probes. Training and calibrating examiners decrease but do not eliminate examiner error. Probing errors also result from patient characteristics, such as anatomical differences in tooth contour, particularly in furcation areas. Probing error varies for different sites within the mouth [69]. Patient discomfort can also result in erroneous measurements [69]. Measurement error limits the ability to identify subtle differences in clinical values, which may be important in early disease detection and intervention. These errors diminish the likelihood of accurately identifying etiological factors correlated with disease progression. Finally, a fundamental limitation is that probing cannot identify disease activity status – which is important, given the cyclical and intermittent nature of periodontal disease activity.

OCT is particularly well suited for periodontal diagnosis, generating ultrahigh resolution cross-sectional images of dental tissues. It has been shown that OCT reliably depicts soft and hard tissue boundaries of the periodontium [70]. Moreover, OCT offers a precision of measurement that is not possible with traditional diagnostic methods. All current periodontal probing methods rely on physical measurements at single points along the tooth surface. To characterize a tooth using current probing methods, points are usually assessed. Thus, all current methods are not only tedious but also assume a direct relationship between these linear point measurements and the area of root surface attachment. OCT, on the other hand, provides rapid, consistent, and reproducible images of the surface topography, pocket morphology, and attachment level that is digitally recorded. These images pinpoint with greater accuracy sites of disease progression. OCT also provides quantitative information regarding the thickness and character of the gingiva, root surface irregularities, and the distribution of subgingival calculus. OCT may delineate changes in the optical properties or structural integrity of the gingival fiber. Comparing OCT images over time should allow clinicians to quickly detect potential sites of disease progression, perhaps even before attachment is lost. OCT images should prove to be extremely valuable in maintaining sites during supportive periodontal therapy. Electronic and visual recording of clinical data avoids subjectivity and transcription error that is associated with current metric techniques [65]. OCT has the capacity to detect disease in the soft tissue early, before bone resorption occurs. When Doppler algorithms are combined with OCT, blood flow can be localized and qualified (Fig. 74.12) offering the exciting potential to distinguish active from non-active periodontitis. Blood flow measurements may

Fig. 74.11 (continued) (*C*); *Center right*: post-sealant 3D OCT image with carious occlusal pit (*CP*) indicated by *white arrow*; RHS: post-sealant 2D OCT image where *white arrow* indicates EDJ and *yellow arrow* indicates caries. P-occlusal pit; *E* enamel, *D* dentin; *S* sealant, *C* caries, *CP* carious pit, *EDJ* enamel-dentin junction [58]

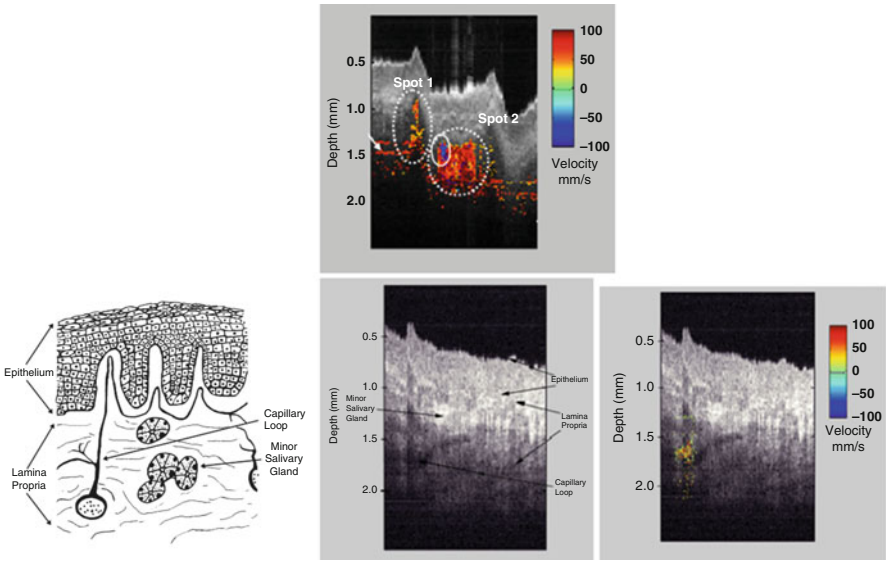

Fig. 74.12 Doppler OCT illustrating blood flow in a human lip [72]

also help elucidate the pathogenesis of periodontitis associated with diabetes and smoking [71, 72].

In a study by Baek et al., the successful use of OCT for monitoring periodontal ligament changes during orthodontic tooth movements was reported in rats [73] (Fig. 74.13). Clinical periodontal probing depth has been shown to correlate well with that measured in OCT images. The midfacial surface of 14 non-restored teeth (1 mandibular and 3 maxillary incisors, 4 maxillary and 6 mandibular premolars) was imaged using a prototype OCT system (1,310-nm wavelength light source, 14 mW, 95 dB dynamic range, 0.46 numerical aperture). Following OCT imaging, probing depths were measured in duplicate using a Michigan 0 probe. Important anatomic features including soft tissue surface contour, gingival crest, periodontal sulcus, and DEJ were identified in OCT images of all of the teeth examined. The cementoenamel junction was identified in 18 of the 28 images; the alveolar bone was presumptively identified in 20 of the 28 images. Probing depth as measured in OCT images was strongly correlated to probing depth as measured by conventional probing measurement ($r = 0.83$; $p < 0.05$). The midfacial surfaces of two restored teeth were imaged (1 maxillary molar, 1 maxillary premolar). Restoration margins and internal restoration contours were visualized and did not interfere with interpretation of OCT images of soft tissue landmarks.

Similarly, an all fiber-optic clinical OCT system was used to obtain 12-mm occlusal-apical OCT images of eight premolars in four healthy volunteers. Images were made in duplicate at the mesial facial line angle. This system employed a 6 mW, 1,310-nm light source and produced images that had an axial resolution of 21 μm. The images of periodontal tissues were similar to those obtained in

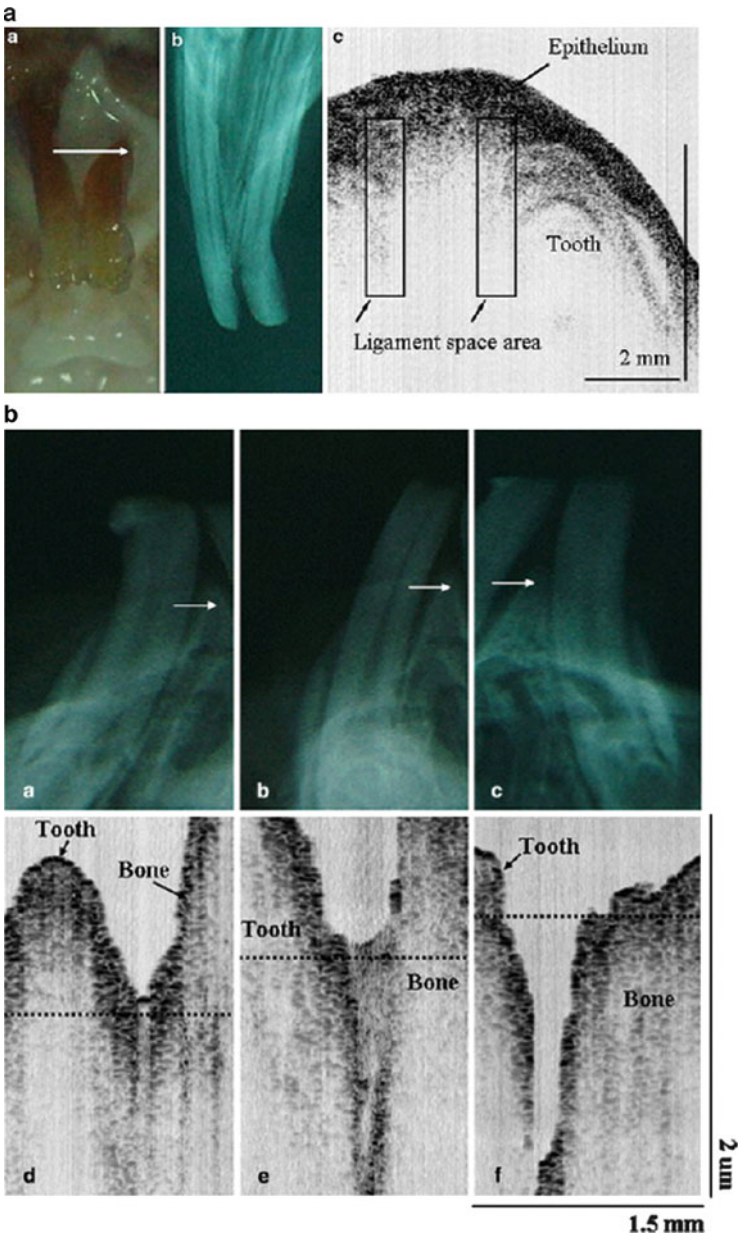

Fig. 74.13 Maxillary anterior tooth of a white rat. (**a**) shows data from the control group to which no orthodontic force was applied: (*a*) optical photograph; (*b*) radiographic image; (*c*) OCT image [73]. (**b**) shows radiographic (*top*) and OCT images (*bottom*) of the maxillary anterior teeth under several orthodontic forces: (*a*, *d*) 5 gf; (*b*, *e*) 10 gf; (*c*, *f*) 30 gf forces, respectively. The two-dimensional OCT image in the *bottom* was taken along the *arrow* direction in each of the *top* (radiographic) figures [73]

previous studies. Characteristic signals representing the sulcus and attached tissues were identified in all images. Premolar sulcular depth as determined from the OCT images ranged from 1.1 to 2.5 and was strongly correlated with probing depth ($r = 0.88$; $p < 0.05$). We defined attached tissues in the OCT images by a uniform signal intensity with no discernable tissue interfaces that extended from the base of the sulcus to the alveolar crest. Measurement of attached tissues in the OCT images ranged from 1.1 to 3.8 mm. The lowest values for attached tissues were found in three teeth with coronal restorations. Signals presumptively identified as the alveolar crest were identified in 60 of the 64 images. The thickness of the gingiva covering the alveolar crest ranged from 0.4 to 1.4 mm. Two teeth had characteristic signals representative of the root surface covered by a thin mucosal tissue; these sites were presumptively identified as fenestration defects. While the OCT images of the root surface are unmistakable, definitive proof of OCT to image fenestration defects requires further investigation. The results of this study, however, convincingly demonstrate capacity of OCT to determine gingival thickness and the shape and contour of the alveolar crest. Visualizing these anatomical features represents a significant contribution to periodontal surgical treatment planning.

74.3 Dental Implants

Endosseous dental implants have been established as a predictable treatment modality for the replacement of missing teeth. While only 2 % of implants fail within the first year, the failure rate rises to 10 % at 5 years and nearly 15 % at 10 years [74, 75]. A successful implant is defined as one that is not mobile and has no peri-implant radiolucencies, no clinical signs of infection, and no discomfort or pain [76–89]. Favorable vertical soft tissue relationships have been demonstrated to be important in the success of dental implants, particularly in maintaining crestal bone height [83]. Peri-implantitis is defined as an inflammatory process affecting the tissues around an osseointegrated implant in function, resulting in progressive loss of supporting bone around the implant [82–84]. The prevalence of peri-implantitis is unknown, although researchers estimate that it ranges from 8 % to as high as 44 % [82–84]. The diagnosis of peri-implantitis is complicated because adequate diagnostic methods to evaluate soft tissues are unavailable and because it is difficult to monitor crestal bone loss around implants. Ideally, implants should lose minimal bone. The implant is at significant risk when more than one-half of the implant height has lost crestal contact [74, 88].

Studies have shown that once peri-implant inflammation is established, it is difficult to eradicate. Unequivocally, any sign of peri-implantitis threatens the longevity of implant restorations and represents a significant health care cost. For these reasons, after implant placement, patients should be examined at regular intervals to evaluate clinical signs and symptoms of peri-implant disease and to receive maintenance therapy [78, 82, 89].

Current implant diagnostic procedures rely on visual estimates of clinical signs of inflammation or single-point physical measurements, such as probing depth.

These techniques lack sufficient sensitivity to detect peri-implantitis at an early stage. Current methods are also subject to high levels of measurement error, and extensive clinical calibration of examiners is required to achieve inter-examiner reliability. The inability to detect problems early jeopardizes effective care. More sensitive tests are needed to understand the causes of late implant failure, to reliably evaluate differences in clinical outcomes between various implant systems, or to evaluate the success of therapeutic interventions for the treatment of peri-implantitis [82, 90].

74.3.1 Expected Improvement of Implant Diagnoses Using OCT

OCT can be used clinically to detect early peri-implantitis with greater sensitivity than current diagnostic methods (Figs. 74.13a, b), with images providing rapid, consistent, and reproducible documentation of peri-implant soft tissue morphology and attachment level. Quantitative information regarding microstructural architecture including the character of the gingiva as well as implant soft tissue relationships is generated. More importantly, OCT identifies the earliest signs of inflammation, so minimal that clinical examination is unlikely to distinguish them. Comparing OCT images over time should prove to be extremely valuable in monitoring health in implant sites during maintenance therapy. Moreover, OCT imaging offers the exciting potential to detect peri-implantitis before significant osseous destruction occurs.

Histological studies in animals have shown that gingival connective tissue forms a scar-like fibrous connective tissue adjacent to titanium implant surfaces, while peri-implantitis is characterized by a disorganized connective tissue containing more vascular elements. Our preliminary data demonstrate that in OCT images of healthy implant sites, collagen appears well organized, and, because of its birefringent nature, it produces a characteristic high OCT signal intensity. OCT images of soft tissue surrounding failing implants are markedly different from images of healthy implant sites and are characterized by linear signal deficits, low-intensity collagen signals, and pronounced increases in vascular elements. To evaluate the feasibility of OCT imaging for implant diagnoses, we conducted preliminary studies in three patients with failing implants. Figure 74.14a demonstrates a 6-mm OCT image made from the midfacial surface of a healthy dental implant site. The peri-implant tissues show no clinical signs of inflammation, and the probing depth measured 1 mm. Figure 74.14b is an OCT image of a plasma-coated IMZ implant. This image illustrates the characteristic findings associated with failing implants, low collagen signal, and increased vascular elements.

OCT will improve clinical evaluation of peri-implant soft tissues and will provide significant advantages over existing diagnostic procedures. Two- or three-dimensional OCT images can depict the topography of the implant sulcus and the relationship of implant soft tissue interfaces. These images can be stored in the patient record and be used to monitor implant health over time. The imaging process is painless, and patient acceptance is far greater than for other dental procedures. Because OCT is noninvasive, it can be performed repeatedly without any risk to the patient.

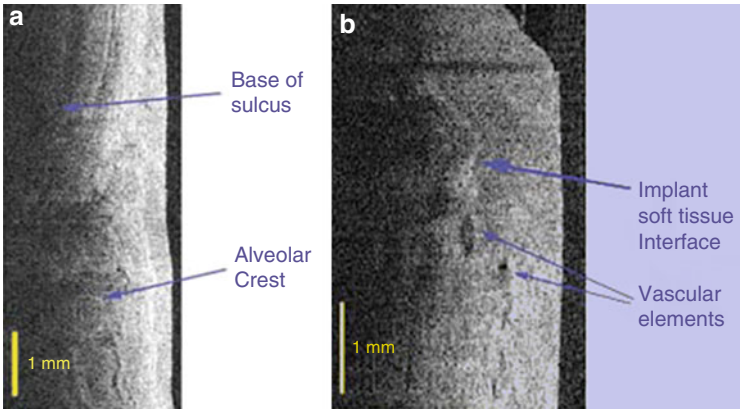

Fig. 74.14 (**a**) OCT image of a healthy dental implant. (**b**) OCT image of failing dental implant

74.4 Oral Dysplasia and Malignancy

According to the American Cancer Society, 1,220,100 patients were diagnosed with cancer in the year 2000. In the same year, 552,200 persons were expected to succumb to cancer [91]. Despite significant advances in cancer treatment, early detection of oral cancer and its curable precursors remains the best way to ensure patient survival and quality of life. Oral cancer will claim approximately 10,000 lives in the USA this year [92, 93]. Accounting for 96 % of all oral cancers, squamous cell carcinoma is usually preceded by dysplasia presenting as white epithelial lesions on the oral mucosa (leukoplakia). Leukoplakias develop in 1–4 % of the population [94]. Malignant transformation, which is quite unpredictable, occurs in 1–40 % of leukoplakias over 5 years. Dysplastic lesions in the form of erythroplakias carry a risk for malignant conversion of 90 %. Tumor detection is complicated by a tendency toward field cancerization, leading to multicentric lesions [94]. Current techniques require surgical biopsy of lesions, which are often benign, yet they detect malignant change too late. Of all oral cancer cases documented by the National Cancer Institute Surveillance, Epidemiology, and End Results Program, advanced lesions outnumbered localized lesions more than 2:1. Five-year survival rate is 75 % for those with localized disease at diagnosis but only 16 % for those with cancer metastasis [92, 93].

Two basic facts indicate that early detection of oral malignancy should be possible to a far greater extent than is currently seen:

1. ***Oral cancer is predominantly preceded by white or red lesions which are visible to the naked eye and which are often present for a considerable period of time prior to transformation.*** A noninvasive diagnostic modality would permit monitoring of these lesions at regular intervals and detection of transformation and any treatment needs at a very early, relatively harmless stage.

2. ***High-risk populations are clearly defined.*** Tobacco use, alcohol abuse, urban environment, African-American background, poor diet, and frequent exposure to sunlight are primary predisposing factors for oral malignancy [95, 96]. A fast, mobile, relatively inexpensive noninvasive diagnostic modality would permit regular screening for oral lesions and subsequent transformation at an early, relatively harmless stage.

74.4.1 Existing and Emerging Techniques for Oral Diagnosis

1. **Visual examination and biopsy** Oral cancer can be detected by dentists and physicians, but physicians do not routinely inspect their patients for suspicious oral lesions, and dentists are also remiss in the early diagnosis and referral for oral cancer. Since 11 % of dentists and 45 % of physicians do not feel adequately trained to complete an effective oral cancer examination, this results in their failure to examine for oral cancer [96]. The current approach to detecting the transformation of leukoplakia/erythroplakia to squamous cell carcinoma is regular surveillance combined with biopsy or surgical excision. However, visual examination provides very poor diagnostic accuracy, and biopsy techniques are invasive and unsuitable for regular screening of high-risk sectors of the population. Adequate visual identification and biopsy of all such lesions to ensure that they are all recognized and diagnosed are difficult, given the often multifocal nature of oral malignancy [93].
2. **Vital staining** Several studies have investigated the use of vital staining with agents such as Lugol iodine, toluidine blue, and tolonium chloride for detection of oral malignancy. Although the sensitivity of these agents in the hands of experts generally approximates 90 %, specificity of these agents is poor; sensitivity rapidly decreases when this modality is used by nonexperts such as screeners in field units. Extensive clinical experience is necessary to perform these examinations adequately [97–103].
3. **Oral brush cytology** Using cytological examination of "brush biopsy" samples as a noninvasive method of oral diagnosis has been shown to provide moderate sensitivity levels of detection of oral epithelial dysplasia or squamous cell carcinoma (70–90 %) but poor specificity (3–44 %). Thus, this approach is of limited diagnostic value without augmentation by traditional biopsy [103–105].
4. **Photosensitizers** Topical or systemic application of photosensitizers can render pathologic tissues fluorescent when exposed to specific wavelengths of light [106]. While several studies have demonstrated the use of porphyrins as photosensitizers, their accumulation in skin after systemic administration can cause phototoxic reactions upon exposure to sunlight [107, 108]. An alternative approach is to stimulate synthesis of photosensitizing agents in situ with a photoinactive precursor. The photosensitizer protoporphyrin IX (PpIX) is an immediate precursor of heme in the biosynthetic pathway for heme. In certain types of cells and tissues, the rate of PpIX synthesis is determined by the rate of

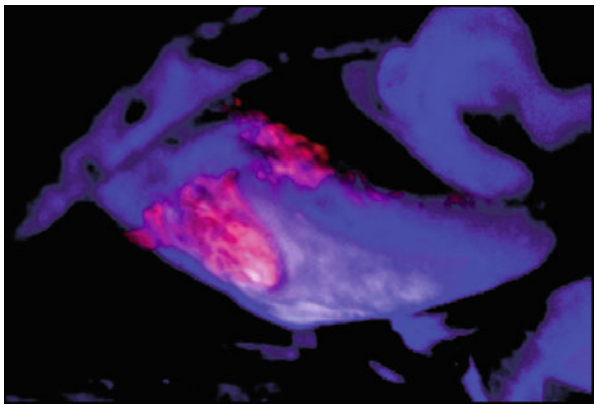

Fig. 74.15 Fluorescence imaging of squamous cell carcinoma of the tongue (*reddish color*) 3 h after topical application of Photofrin® [109]

synthesis of 5-aminolevulinic acid (ALA), which in turn is regulated via a feedback control mechanism governed by the concentration of free heme. The presence of exogenous ALA bypasses the feedback control of this process, inducing the intracellular accumulation of photosensitizing concentrations of PpIX. A selective accumulation of PpIX occurs in areas of increased metabolism such as tumor cells [106]. The resulting tissue-specific photosensitization provides the basis for using ALA-induced PpIX for photodynamic diagnosis and therapy, whereby far lower light doses are used for photodynamic diagnosis. This technique has shown great promise in animal and human studies for head and neck cancers including oral lesions [108–111] (Fig. 74.15). Limitations include the localization of induced fluorescence to the surface layers of the epithelium and the fluorescence caused by common coexisting clinical pathologies such as candidal superinfection, hyperplasia, atrophy, and ulceration.

5. **Spectroscopy** Various types of optical spectroscopy have been investigated to effect a noninvasive, real-time in situ assessment of tissue pathology. All of these methods have one basic principle in common: the optical spectrum of a tissue contains information about the biochemical composition and/or the structure of the tissue which conveys diagnostic information. Malignancy-related biochemical and morphologic changes perturb tissue absorption, fluorescence, and scattering properties. The biochemical information can be obtained by measuring absorption/reflectance, fluorescence, or Raman scattering signals. Structural and morphological information may be obtained by techniques that assess the elastic-scattering properties of tissue [112, 113].

   Reflectance spectroscopy can probe changes in epithelial nuclei that are important in precancer detection, such as mean nuclear diameter, nuclear size distribution, and nuclear refractive index [114]. Applications under investigation include the cervix [115], skin [116], colon [117], oral cavity [114], and esophagus [118].

   Fluorescence spectroscopy can probe changes in epithelial cell metabolism, by assessing mitochondrial fluorophores, and epithelial-stromal

interactions, by assessing the decrease in collagen cross-link fluorescence that occurs with precancer. Areas of application include the cervix, skin, bladder, oral cavity, and esophagus [113, 118–132].

Raman spectroscopy uses laser excitation and the scattering effect is observed in the target tissues. Inelastic scattering results in a frequency shift in the reflected Raman spectra, which are functions of the type of molecules in the sample. Thus, the Raman spectra hold useful information on the different chemical compounds. Raman spectroscopy has been investigated for medical diagnosis applications in general and for the investigation of sites such as the skin, cervix, larynx, esophagus, and colon [115, 119, 133–144].

Significant challenges to the use of diagnostic spectroscopy include the often low signal-to-noise ratio, difficulty in identifying the precise source of signals, data quantification issues, and establishing definitive diagnostic milestones and endpoints. Limited tissue penetration and concerns about mutagenicity when using UV light present further clinical challenges. The abundance of data/information generated in association with our incomplete understanding of the carcinogenesis process render data analysis and interpretation very complex. Many studies have been performed on small numbers of small biopsy samples which do not necessarily translate directly or accurately to the clinical situation.

6. **Optical coherence microscopy** This modality combines the subcellular resolution of confocal microscopy with the increased sensitivity and penetration depth of optical coherence tomography (OCT) to noninvasively acquire details similar to that available in histologic tissue evaluation. Typically, a resolution of 2 μm and a 200- to 500-μm field of view at a penetration depth of up to 600 μm are reported in the literature [145–150]. This suggests that OCM has the potential to image epithelial tissues with the subcellular resolution needed to assess their pathologic state. Challenges include the small field of view, limited penetration depth (although better than confocal reflectance microscopy), and the need for an intraoral probe.
7. **Confocal reflectance microscopy** In vivo confocal imaging resembles histological tissue evaluation, except that three-dimensional subcellular resolution is achieved noninvasively and without stains. In epithelial structure, resolution of 1 μm has been achieved with a 200–400-μm field of view. In skin, where cytoplasmic melanin provides a strong source of backscattering, confocal microscopes have captured morphologic changes in cytologic structure and visualized microvasculature in both basal cell carcinomas and melanomas [151–158]. In amelanotic epithelial tissues, where cell nuclei provide the primary source of reflected light, recent work showed that reflectance confocal imaging of normal and precancerous cervical tissue can characterize nuclear size, nuclear density, and nuclear-to-cytoplasmic ratio without the need for tissue sectioning or staining. In these ex vivo studies, confocal images were used to discriminate high-grade cervical precancers with a sensitivity of 100 % and a specificity of 91 % in a study of 25 samples [159, 160]. Similarly, nuclear-to-cytoplasmic

differences from images of normal and esophageal cancer cells were used to identify cancer with a diagnostic accuracy of 90 % [161]. Confocal imaging of oral mucosa has resolved subcellular detail in the lip and tongue [162] and oral squamous cell carcinoma from multiple sites [163]. While this technology can provide detailed images of tissue architecture and cellular morphology, a very small field of view and limited penetration depth of 250–500 μm considerably reduce the clinical usefulness of this approach.

74.4.2 OCT Diagnosis

Performing studies in the hamster cheek pouch model and in humans, the macroscopic and vascular status of healthy, dysplastic, and malignant oral mucosa has been imaged using in vivo OCT/ODT. Multiple epithelial and subepithelial layers as well as the presence or absence of basement membrane can be visualized. Epithelial invasion during malignant transformation was clearly identified. Blood vessel presence, size, and localization relative to tumor tissue were visible, and blood flow could be quantified [164, 165]. In oral malignancy, small blood vessels were often seen in close proximity to tumor tissue, and using IHC a progressively increased blood vessel count with decreasing level of tumor differentiation was demonstrated [166, 167].

Movement artifacts during OCT registration in human subjects do not appear to be a problem when using the newer, faster imaging systems. As long as patients are seated comfortably in a clinical chair with headrest and neck support, this was not an issue at all, as evidenced by Fig. 74.16. Epithelium, lamina propria, and basement membrane are clearly visible. Structural appearance in the OCT image parallels histological appearance, showing epithelial thickening, loss of stratification in lower epithelial strata, epithelial downgrowth, and presence of basement membrane in dysplastic tissue (Fig. 74.16).

In a clinical study involving 50 patients with leukoplakia or erythroplakia, oral lesions, pre-standardized clinicians were able to diagnose oral lesions from noninvasive in vivo OCT images with approx. 85 % accuracy vs. the gold standard, surgical biopsy, and histopathology [164]. Another study in 73 patients with 78 suspicious oral lesions identified similar levels of diagnostic accuracy [165]. These data demonstrate the excellent capability of in vivo OCT for detecting and diagnosing oral soft tissue pathologies in patients.

74.5 Future Potential

The potential for OCT-based diagnostics in the oral cavity is excellent. The penetration depth of this modality in oral hard and soft tissues is adequate for most dental applications. Ongoing innovations, such as the development of Fourier-domain OCT, which enable up to 100× faster acquisition of 3D OCT images, and of spectral OCT, which provide enhanced imaging contrast, will permit spatially

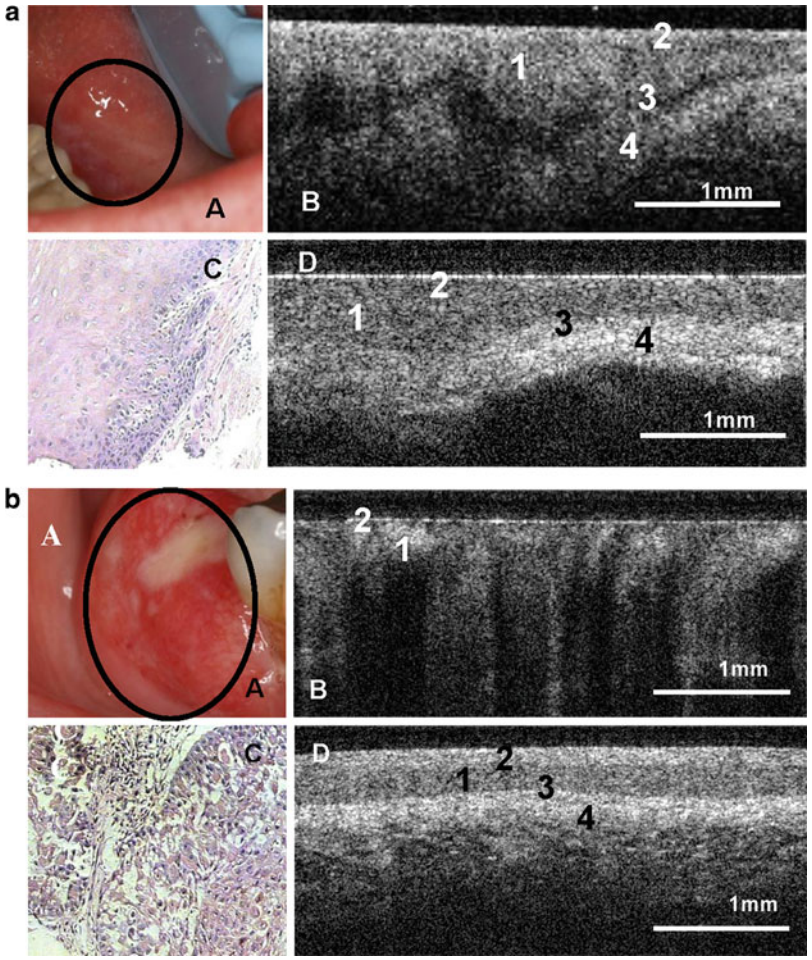

Fig. 74.16 (**a**) Photograph (A), in vivo OCT image (B), and H&E (C) of dysplastic buccal mucosa. In vivo OCT image of normal buccal Mucosa is shown in (D). (**b**) Photograph (A), in vivo OCT image (B), and H&E (C) of alveolar ridge with squamous cell carcinoma. In vivo OCT image of normal alveolar Mucosa is shown in (D). 1-stratified squamous epithelium, 2-keratinized epithelial surface layer, 3-basement membrane, 4-subucosa

resolved detection and quantification of changes within the tissues such as demineralization through their spectroscopic properties. Emerging MEMS-based and 3D techniques are significant factors permitting enhanced speed and effectiveness of the images obtained. Based on the data available to date, direct clinical in vivo imaging shows great potential for improving diagnostic capabilities in the oral cavity for applications ranging from decay, through periodontal disease, to oral malignancy.

References

1. B.W. Colston, M.J. Everett, L.B. DaSilva, L.L. Otis, P. Stroeve, H. Nathel, Imaging of hard and soft tissue in the oral cavity by optical coherence tomography. Appl. Optics **37**(16), 3582–3585 (1998)
2. B.W. Colston Jr., S. Sathyam, L.B. DaSilva, M.J. Everett, P. Stroeve, L.L. Otis, Dental OCT. Opt. Express **3**, 230–238 (1998)
3. L.L. Otis, M.J. Everett, U.S. Sathyam, B.W. Colston Jr., Optical coherence tomography: a new imaging technology for dentistry. J. Am. Dent. Assoc. **131**(4), 511–514 (2000)
4. A. Nanci, A.R. Ten Cate, Ten Cate's oral histology: development, structure, and function (Elsevier Mosby, St. Louis, MO, 2013), pp. 239–256
5. A. Nanci, A. R. Ten Cate, Ten Cate's oral histology: development, structure, and function (Elsevier Mosby, St. Louis, MO, 2013), pp. 169–217
6. L. Otis, Y. Chen, Q. Zhu, Characterization of dentin by optical coherence tomography. J. Dent. Res. **82**, A 3979 (2004)
7. J.A. Izatt, K. Kobayashi, M.V. Sivak, J.K. Barton, A.J. Welch, Optical coherence tomography for biodiagnostics. Opt. Photon. News **8**, 41–47 (1997)
8. Z. Ding, High-resolution optical coherence tomography over a large depth range with an axicon lens. Opt. Lett. **27**, 4 (2002)
9. L.L. Otis, B.W. Colston Jr., M.J. Everett, H. Nathel, Dental optical coherence tomography: a comparison of two in vitro systems using a light source at 1310 nm. Dentomaxillofac. Radiol. **29**(2), 85–89 (2000)
10. Y. Pan, Z. Li, T. Xie, C.R. Chu, Hand-held arthroscopic optical coherence tomography for in vivo high-resolution imaging of articular cartilage. J. Biomed. Opt. **8**(4), 648–654 (2003)
11. W.G. Jung, J. Zhang, L. Wang, P. Wilder-Smith, Z. Chen, D. McCormick, N.C. Tien, Three-dimensional optical coherence tomography employing A 2-axis microelectromechanical scanning mirror. IEEE Journal of Selected Topics in Quantum Electronics 11, 806–810 (2005)
12. J.M. Zara, S. Yazdanfar, K.D. Rao, J.A. Izatt, S.M. Smith, Electrostatic micromachine scanning mirror for optical coherence tomography. Opt. Lett. **28**, 828–830 (2003)
13. P. Tran, D.S. Mukai, M. Brenner, Z. Chen, In vivo endoscopic optical coherence tomography using rotational MEMS probe. Opt. Lett. **29**, 1236–1239 (2004)
14. Y. Wang, M. Bachman, G.P. Li, S. Guo, B. Wong, Z. Chen, Low-voltage polymer-based scanning cantilever for in vivo optical coherence tomography. Opt. Lett. **30**, 53–55 (2005)
15. W.G. Jung, J. Zhang, L. Wang, Z. Chen, D.T. McCormick, N.C. Tien, Three-dimensional endoscopic optical coherence tomography by use of a two-axis microelectromechanical scanning mirror. Appl. Phys. Lett. **88**, 163901–163903 (2006)
16. W.G. Jung, L. Zhang, J. Wang, Z. Chen, D.T. McCormick, N.C. Tien, Three-dimensional optical coherence tomography employing a 2-axis microelectromechanical scanning mirror. IEEE J. Sel. Top. Quantum Electron. **11**, 806–810 (2005)
17. A.D. Aguirre, P.R. Hertz, Y. Chen, J.G. Fujimoto, W. Piyawattanametha, L. Fan, M.C. Wu, Two-axis MEMS scanning catheter for ultrahigh resolution three-dimensional and en face imaging. Opt. Express **15**, 2445–2453 (2007)
18. J.T.W. Yeow, V.X.D. Yang, A. Chahwan, M.L. Gordon, B. Qi, I.A. Vitkin, B.C. Wilson, A.A. Goldenberg, Micromachined 2-D scanner for 3-D optical coherence tomography. Sensors Actuators A **117**, 331–340 (2005)
19. X. Liu, M.J. Cobb, Y. Chen, M.B. Kimmey, X. Li, Rapid-scanning forward-imaging miniature endoscope for real-time optical coherence tomography. Opt. Lett. **29**(15), 1763–1765 (2004)
20. S. Moon, S.W. Lee, M. Rubinstein, B.J. Wong, Z. Chen, Semi-resonant operation of a fiber-cantilever piezotube scanner for stable optical coherence tomography endoscope imaging. Opt. Express **18**(20), 21183–21197 (2010)
21. S.A. Boppart, B.E. Bouma, C. Pitris, J.G. Tearney, J.G. Fujimoto, M.E. Brezinski, Forward-imaging instruments for optical coherence tomography. Opt. Lett. **22**(21), 1618–1620 (1997)

22. N.R. Munce, A. Mariampillai, B.A. Standish, M. Pop, K.J. Anderson, G.Y. Liu, T. Luk, B.K. Courtney, G.A. Wright, I.A. Vitkin, V.X. Yang, Electrostatic forward-viewing scanning probe for Doppler optical coherence tomography using a dissipative polymer catheter. Opt. Lett. **33**(7), 657–659 (2008)
23. E.J. Min, J. Na, S.Y. Ryu, B.H. Lee, Single-body lensed-fiber scanning probe actuated by magnetic force for optical imaging. Opt. Lett. **34**(12), 1897–1899 (2009)
24. L. Huo, J. Xi, Y. Wu, X. Li, Forward-viewing resonant fiber-optic scanning endoscope of appropriate scanning speed for 3D OCT imaging. Opt. Express **18**(14), 14375–14384 (2010)
25. M.H. Niemz, *Laser-tissue interactions* (Springer, Berlin, 1996), pp. 178–195
26. A. Nanci, A.R. Ten Cate, Ten Cate's oral histology: development, structure, and function (Elsevier Mosby, St. Louis, MO, 2013), pp. 462–465.
27. A. Lussi, Validity of diagnostic and treatment decisions of fissure canes. Caries Res. **25**, 296–303 (1991)
28. A. Wenzel, N. Pitts, E.H. Verdonschott, H. Kalsbeek, Developments in radiographic caries diagnosis. Dent **21**, 131–140 (1993)
29. R.B. Nytun, M. Raadal, I. Espelid, Diagnosis of dentin involvement in occlusal caries based on visual and radiographic examination of the teeth. Scand. J. Dent. Res. **100**, 144–148 (1992)
30. K.L. Weerheijm, H.J. Groen, A.J.J. Bast, J.A. Kieft, M.A.J. Eijkman, W.E. van Amerongen, Clinically Undetected occlusal dentine caries: a radiographic comparison. Caries Res. **26**, 305–309 (1992)
31. K.R. Ekstrand, D.N. Ricketts, C. Longbottom, N.B. Pitts, Visual and tactile assessment of arrested initial enamel lesions. Caries Res. **39**(3), 173–177 (2005)
32. K.R. Ekstrand, I. Kuzmina, L. Bjomdal, A. Thyistrup, Relationship between external and histologic features of progressive stages of caries in the occlusal fossa. Caries Res. **29**, 243–250 (1995)
33. K.R. Ekstrand, D.N. Ricketts, E.A. Kidd, Do occlusal carious lesions spread laterally at the enamel-dentin junction? A histolopathological study. Clin. Oral Investig. **2**(1), 15–20 (1998)
34. A. Wenzel, E.H. Verdonschot, G.J. Truin, K.G. Konig, Accuracy of visual inspection, fiber-optic transillumination, and various radiographic image modalities for the detection of occlusal caries in extracted non-cavitated teeth. J. Dent. Res. **71**(12), 1934–1937 (1992)
35. B.T. Amaechi, S.M. Higham, A.G.H. Podoleanu, J.A. Rogers, D.A. Jackson, Use of optical coherence tomography for assessment of dental caries: quantitative procedure. J. Oral Rehabil. **28**(12), (2001)
36. B.T. Amaechi, A. Podoleanu, S.M. Higham, D.A. Jackson, Correlation of quantitative light-induced fluorescence and optical coherence tomography applied for detection and quantification of early dental caries. J. Biomed. Opt. **8**(4), 642–647 (2003)
37. A.C. Ko, L.P. Choo-Smith, M. Hewko, L. Leonardi, M.G. Sowa, C.C. Dong, P. Williams, B. Cleghorn, Ex vivo detection and characterization of early dental caries by optical coherence tomography and Raman spectroscopy. J. Biomed. Opt. **10**(3), 031118 (2005)
38. M.G. Sowa, D.P. Popescu, J.R. Friesen, M.D. Hewko, L.P. Choo-Smith, A comparison of methods using optical coherence tomography to detect demineralized regions in teeth. J. Biophotonics **4**(11–12), 814–823 (2011)
39. B.T. Amaechi, A.G. Podoleanu, G. Komarov, S.M. Higham, D.A. Jackson, Quantification of root caries using optical coherence tomography and microradiography: a correlational study. Oral Health Prev. Dent. **2**(4), 377–382 (2004)
40. L.S. de Melo, R.E. de Araujo, A.Z. Freitas, D. Zezell, N.D. Vieira, J. Girkin, A. Hall, M.T. Carvalho, A.S. Gomes, Evaluation of enamel dental restoration interface by optical coherence tomography. J. Biomed. Opt. **10**(6), 64027 (2005)
41. P. Ngaotheppitak, C.L. Darling, D. Fried, Measurement of the severity of natural smooth surface (interproximal) caries lesions with polarization sensitive optical coherence tomography. Lasers Surg. Med. **37**(1), 78–88 (2005)

42. Y. Chen, L.L. Otis, D.Q. Piao, Q. Zhu, Characterization of dentin enamel and carious lesion by a polarization-sensitive optical coherence tomography system. Appl. Optics **44**(11), 2041–2048 (2005)
43. D. Fried, J. Xie, S. Shafi, J.D. Featherstone, T.M. Breunig, C. Le, Imaging caries lesions and lesion progression with polarization sensitive optical coherence tomography. J. Biomed. Opt. **7**(4), 618–627 (2002)
44. A. Baumgartner, S. Dichtl, C.K. Hitzenberger, H. Sattmann, B. Robl, A. Moritz, A.F. Fercher, W. Sperr, Polarization-sensitive optical coherence tomography of dental structures. Caries Res. **34**(1), 59–69 (2000)
45. H. Kang, C.L. Darling, D. Fried, Nondestructive monitoring of the repair of enamel artificial lesions by an acidic remineralization model using polarization-sensitive optical coherence tomography. Dent. Mater. **28**(5), 488–494 (2012)
46. T. Louie, C. Lee, D. Hsu, K. Hirasuna, S. Manesh, M. Staninec, C.L. Darling, D. Fried, Clinical assessment of early tooth demineralization using polarization sensitive optical coherence tomography. Lasers Surg. Med. **42**(10), 738–745 (2010)
47. A. Milosevic, Toothwear: aetiology and presentation. Dent. Update **25**, 6–11 (1998)
48. J. Meurmann, J. Toskala, P. Nuutinien, E. Klemetti, Oral and dental manifestations in gastroesophageal reflux disease. Oral Surg. Oral Med. Oral Pathol. **78**, 583–589 (1994)
49. B. Gregory-Head, D.A. Curtis, Erosion caused by gastroesophageal reflux: diagnostic considerations. J. Prosthodont. **6**, 278–285 (1997)
50. D.W. Bartlett, D.F. Evans, B.G. Smith, The relationship between gastro-oesophageal reflux disease and dental erosion. J. Oral Rehabil. **23**, 289–297 (1996)
51. C.H. Wilder-Smith, P. Wilder-Smith, H. Kawakami-Wong, J. Voronets, K. Osann, A. Lussi, Quantification of dental erosions in patients with GERD using optical coherence tomography before and after double-blind, randomized treatment with esomeprazole or placebo. Am. J. Gastroenterol. **104**(11), 2788–2795 (2009). doi:10.1038/ajg.2009.441
52. H. Shemesh, G. van Soest, M.K. Wu, P.R. Wesselink, Detection of root surface fractures with swept-source optical coherence tomography (SS-OCT). Photomed. Laser Surg. **31**(1), 23–27 (2013). doi:10.1089/pho.2012.3383
53. T. Yoshioka, H. Sakaue, H. Ishimura, A. Ebihara, H. Suda, Y. Sumi, Diagnosis of vertical root fractures with optical coherence tomography. J. Endod. **34**(6), 739–742 (2008)
54. G.Q. Monteiro, M.A. Montes, A.S. Gomes, C.C. Mota, S.L. Campello, A.Z. Freitas, Marginal analysis of resin composite restorative systems using optical coherence tomography. Dent. Mater. **27**(12), e213–e223 (2011)
55. T.A. Bakhsh, A. Sadr, Y. Shimada, J. Tagami, Y. Sumi, Non-invasive quantification of resin-dentin interfacial gaps using optical coherence tomography: validation against confocal microscopy. Dent. Mater. **27**(9), 915–925 (2011)
56. L.L. Otis, J.C. Meiers, Refraction artifacts cause spatial distortion in OCT images. J. Dent. Res. **79**(SI), 456 (2000)
57. L.L. Otis, R.I. al-Sadhan, J. Meiers, D. Redford-Badwal, Identification of occlusal sealants using optical coherence tomography. J. Clin. Dent. **14**(1), 7–10 (2003)
58. J.S. Holtzman, K. Osann, J. Pharar, K. Lee, Y.C. Ahn, T. Tucker, S. Sabet, Z. Chen, R. Gukasyan, P. Wilder-Smith, Ability of optical coherence tomography to detect caries beneath commonly used dental sealants. Lasers Surg. Med. **42**(8), 752–759 (2010)
59. R.S. Jones, M. Staninec, D. Fried, Imaging artificial caries under composite sealants and restorations. J. Biomed. Opt. **9**(6), 1297–1304 (2004)
60. L.L. Otis, B.W. Colston, M.J. Everett, Optical coherence tomography: a novel assessment of coronal restorations. J. Dent. Res. **77**, 824 (1998)
61. L.L. Otis, B.W. Colston, M.J. Everett, Optical coherence topography: a novel assessment of composite wear. J. Dent. Res. **77**, 276 (1998)
62. A. Badersten, R. Nilveus, J. Egelberg, Reproducibility of probing attachment level measurements. J. Clin. Periodontol. **11**, 475–485 (1984)

63. G.C. Armitage, G.K. Svanbern, H. Loe, Microscopic evaluation of clinical measurements of connective tissue attachment levels. J. Clin. Periodontol. **4**(3), 173–190 (1977)
64. U. van der Velden, Errors in the assessment of pocket depth in vitro. J. Clin. Periodontol. **5**, 182–187 (1978)
65. H. Kingman, H. Loe, A. Anerun, Boysen, Errors in measuring parameters associated with periodontal health and disease. J. Periodontol. **62**, 77–486 (1991)
66. M.K. Jeffcoat, M.S. Reddy, A comparison of probing and radiographic methods for detection of periodontal disease progression. Curr. Opin. Dent. **1**, 45–51 (1991)
67. M.C.K. Yang, Y.Y. Namgung, R.G. Marks, I. Magnusson, W.B. Clark, Change detection on longitudinal data in periodontal research. J Periodont Res **28**, 152–160 (1993)
68. M.A. Espeland, U.E. Zappa, P.E. Hogan, C. Simona, H. Graf, Cross-sectional and longitudinal reliability for clinical measurement of attachment loss. J. Clin. Periodontol. **18**, 126–133 (1991)
69. M.J. Novak, Diagnosis of periodontal diseases: reaction paper. Adv. Dent. Res. **5**, 37–40 (1991)
70. L.L. Otis, D. Piao, Q. Zhu, Optical coherence tomography of oral soft tissues. J Acad Laser Dent **12**(4), 16 (2004)
71. D.Q. Piao, Q. Zhu, L.L. Otis, Doppler angle and flow velocity mapping by combined Doppler shift and Doppler bandwidth measurements in Optical Doppler tomography. Opt. Lett. **28**(13), 1120–1122 (2003)
72. L.L. Otis, D. Piao, C.W. Gibson, Q. Zhu, Quantifying labial blood flow using optical Doppler tomography. Oral Surg. Oral Med. Oral Pathol. Oral Radiol. Endod. **98**, 189–194 (2004)
73. J. Na, B.H. Lee, J.H. Baek, E.S. Choi, Optical approach for monitoring the periodontal ligament changes induced by orthodontic forces around maxillary anterior teeth of white rats. Med. Biol. Eng. Comput. **46**(6), 597–603 (2008)
74. C.E. Misch, *Dental implant prosthetics* (Elsevier Mosby, St. Louis, Mo, 2005)
75. T. Berglundh, L. Persson, B. Klinge, A systematic review of the incidence of biological and technical complications in implant dentistry reported in prospective longitudinal studies of at least 5 years. J. Clin. Periodontol. **29**(Suppl 3), 197–212 (2002)
76. T. Albrektsson, L. Sennerby, Direct bone anchorage of oral implants: clinical and experimental considerations of the concept of osseointegration. Int. J. Prosthodont. **3**(1), 30–41 (1990)
77. D. Buser, H.P. Weber, N.P. Lang, Tissue integration of non-submerged implants. 1-year results of a prospective study with 100 ITI hollow-cylinder and hollow-screw implants. Clin. Oral Implants Res. **1**(1), 33–40 (1990)
78. M. Esposito, J. Hirsch, U. Lekholm, P. Thomsen, Differential diagnosis and treatment strategies for biologic complications and failing oral implants: a review of the literature. Int. J. Oral Maxillofac. Implants **14**(4), 473–490 (1999)
79. C.E. Misch, The implant quality scale: a clinical assessment of the health – disease continuum. Oral Health **88**(7), 15 (1998)
80. R.T. Kao, D.A. Curtis, P.A. Murray, Diagnosis and management of peri-implant disease. J. Calif. Dent. Assoc. **25**(12), 872–880 (1997)
81. M.S. Block, J.N. Kent, Prospective review of integral implants. Dent. Clin. North Am. **36**(1), 27–37 (1992)
82. G.E. Salvi, N.P. Lang, Diagnostic parameters for monitoring peri-implant conditions. Int. J. Oral Maxillofac. Implants **19**(Suppl), 116–127 (2004)
83. A. Mombelli, N.P. Lang, The diagnosis and treatment of peri-implantitis. Periodontol. 2000 **17**, 63–76 (1998)
84. A. Mombelli, Etiology, diagnosis, and treatment considerations in peri-mplantitis. Curr. Opin. Periodontol. **4**, 127–136 (1997)
85. L.J. Heitz-Mayfield, N.P. Lang, Antimicrobial treatment of peri-implant diseases. Int. J. Oral Maxillofac. Implants **19**(Suppl), 128–139 (2004)

86. B. Klinge, A. Gustafsson, T. Berglundh, A systematic review of the effect of anti-infective therapy in the treatment of peri-implantitis. J. Clin. Periodontol. **29**(Suppl 3), 213–225 (2002)
87. A.M. Roos-Jansaker, S. Renvert, J. Egelberg, Treatment of peri-implant infections: a literature review. J. Clin. Periodontol. **30**(6), 467–485 (2003)
88. M.C. Manz, Factors associated with radiographic vertical bone loss around implants placed in a clinical study. Ann. Periodontol. **5**(1), 137–151 (2000)
89. M. Esposito, P. Thomsen, L.E. Ericson, U. Lekholm, Histopathologic observations on early oral implant failures. Int. J. Oral Maxillofac. Implants **14**(6), 798–810 (1999)
90. J.W. Verhoeven, M.S. Cune, C. de Putter, Reliability of some clinical parameters of evaluation in implant dentistry. J. Oral Rehabil. **27**(3), 211–216 (2000)
91. American Cancer Society, *Cancer Facts and Figures* (American Cancer Society, Atlanta, 2000), p. 4
92. J. Regezi, J. Sciubba (eds.), *Oral Pathology* (W.B.Saunders, Philadelphia, 1993), pp. 77–90
93. California Department of Health Services. *Cancer Surveillance Section Annual Report*, March 1999
94. D.P. Slaughter, H.W. Southwick, W. Smejkal, Field cancerization in oral stratified squamous epithelium. Cancer **6**, 963–968 (1953)
95. U.S. Department of Health and Human Services. A National Call to Action to Promote Oral Health http://www.nidr.nih.gov/sgr/nationalcalltoaction.htm. Rockville: Department of Health and Human Services, Public Health Service, Centers for Disease Control and Prevention, National Institutes of Health, National Institute of Dental and Craniofacial Research, May 2003. Report No.: 03-5303
96. P.E. Petersen, T. Yamamoto, Community Improving the oral health of older people: the approach of the WHO Global Oral Health Programme. Dent. Oral Epidemiol. **33**(2), 81–92 (2005)
97. J.B. Epstein, R. Feldman, R.J. Dolor, S.R. Porter, The utility of tolonium chloride rinse in the diagnosis of recurrent or second primary cancers in patients with prior upper aerodigestive tract cancer. Head Neck **25**(11), 911–921 (2003)
98. J.B. Epstein, L. Zhang, M. Rosin, Advances in the diagnosis of oral premalignant and malignant lesions. J. Can. Dent. Assoc. **68**(10), 617–621 (2002)
99. S. Silverman, C. Migliorati, J. Barbosa, Toluidine blue staining in the detection of oral precancerous and malignant lesions. Oral Surg. Oral Med. Oral Pathol. **57**, 379–382 (1984)
100. J. Epstein, C. Scully, U. Spinelli, Toluidine blue and Lugol's iodine solution for the assessment of oral malignant disease and lesions at risk of malignancy. J. Oral Pathol. Med. **21**, 160–163 (1992)
101. Patton LL, The effectiveness of community-based visual screening and utility of adjunctive diagnostic aids in the early detection of oral cancer. Oral Oncol. **41**, 708–723 (2003)
102. M.A. Onofre, M.R. Sposto, C.M. Navarro, Reliability of toluidine blue application in the detection of oral epithelial dysplasia and in situ and invasive squamous cell carcinomas. Oral Surg. Oral Med. Oral Pathol. Oral Radiol. Endod. **91**(5), 535–540 (2001)
103. T.W. Poate, J.A. Buchanan, T.A. Hodgson, P.M. Speight, A.W. Barrett, D.R. Moles, C. Scully, S.R. Porter, An audit of the efficacy of the oral brush biopsy technique in a specialist Oral Medicine unit. Oral Oncol. **40**(8), 829–834 (2004)
104. G.R. Ogden, J.G. Cowpe, M.W. Green, Detection of field change in oral cancer using oral exfoliative cytologic study. Cancer **68**, 1611–1615 (1991)
105. M.P. Rosin, J.B. Epstein, K. Berean, S. Durham, J. Hay, X. Cheng et al., The use of exfoliative cell samples to map clonal genetic alterations in the oral epithelium of high-risk patients. Cancer Res. **57**, 5258–5260 (1997)
106. J.C. Kennedy, R.H. Pottier, Endogenous protoporphyrin IX, a clinically useful photosensitizer for photodynamic therapy. J. Photochem. Photobiol. **14**, 275–292 (1992)
107. R.C.J. Benson, Treatment of diffuse transitional cell carcinoma in situ by whole bladder hematoporphyrin derivative photodynamic therapy. J. Urol. **134**, 675–678 (1985)

108. K. Svanberg, I. Wang, R. Rydell, A. Elner, J. Wennerberg, L. Pais Clemente, E. Cardosa, R. Pratas, M. Pais Clemente, S. Andersson-Engels, S. Svanberg, Fluorescence diagnostics of head and neck cancer utilizing oral administration of δ-Amino Levulinic acid. SPIE **2371**, 129–141 (1995)
109. C.J. Chang, P. Wilder-Smith, Topical application of photofrin for photodynamic diagnosis of oral neoplasms. Plast. Reconstr. Surg. **115**, 1877–1886 (2005)
110. A. Leunig, K. Rick, H. Stepp, R. Gutmann, G. Alwin, R. Baumgartner, J. Feyh, Fluorescence imaging and spectroscopy of 5-aminolevulinic acid-induced protoporphyrin IX for the detection of neoplastic lesions in the oral cavity. Am. J. Surg. **172**(6), 674–677 (1996)
111. C.S. Betz, H. Stepp, S. Arbogast, G. Grevers, R. Baumgartner, A. Leunig, A comparative study of normal inspection, autofluorescence and 5-ALA-induced PPIX fluorescence for oral cancer diagnosis. Int. J. Cancer **97**, 245–252 (2002)
112. I.J. Bigio, S.G. Bown, Spectroscopic sensing of cancer and cancer therapy: current status of translational research. Cancer Biol. Ther. **3**(3), 259–267 (2004)
113. K. Sokolov, M. Follen, R. Richards-Kortum, Optical spectroscopy for detection of neoplasia. Curr. Opin. Chem. Biol. **6**(5), 651–658 (2002)
114. K. Sokolov, R. Drezek, K. Gossage, R. Richards-Kortum, Reflectance spectroscopy with polarized light: is it sensitive to cellular and nuclear morphology. Opt. Expr. **5**, 302–317 (1999)
115. I. Georgakoudi, E. Sheets, M.G. Muller, V. Backman, C.P. Crum, K. Badizadegan, R.R. Dasari, M.S. Feld, G.R. Harrison, Trimodal spectroscopy for the detection and characterization of cervical precancers in vivo. Am. J. Obstet. Gynecol. **186**, 374–382 (2002)
116. I. Georgakoudi, B.C. Jacobson, J. Van Dam, V. Backman, M.B. Wallace, M.G. Muller, Q. Zhang, K. Badizadegan, D. Sun, G.A. Thomas et al., Fluorescence, reflectance, and light-scattering spectroscopy for evaluating dysplasia in patients with Barretts esophagus. Gastroenterology **120**, 1620–1629 (2001)
117. R.J. Nordstrom, L. Burke, J.M. Niloff, J.F. Myrtle, Identification of cervical intraepithelial neoplasia (CIN) using UV-excited fluorescence and diffuse-reflectance tissue spectroscopy. Lasers Surg. Med. **29**, 118–127 (2001)
118. R.A. Weersink, J.E. Hayward, K.R. Diamond, M.S. Patterson, Accuracy of noninvasive in vivo measurements of photosensitizer uptake based on a diffusion model of reflectance spectroscopy. Photochem. Photobiol. **66**, 326–335 (1997)
119. G. Zonios, L. Perelman, V. Backman, R. Manoharan, M. Fitzmaurice, J. Van Dam, M.S. Feld, Diffuse reflectance spectroscopy of human adenomatous colon polyps in vivo. Appl. Opt. **38**, 6628–6637 (1999)
120. R.R. Alfano, D.B. Tata, J. Cordero, P. Tomashefsky, F.W. Longo, M.A. Alfano, Laser induced fluorescence spectroscopy from native cancerous and normal tissue. IEEE J. Quant. Electron. **20**, 1507–1511 (1984)
121. G.A. Wagnieres, W.M. Star, B.C. Wilson, In vivo fluorescence spectroscopy and imaging for oncological applications. Photochem. Photobiol. **68**, 603–632 (1998)
122. N. Ramanujam, Fluorescence spectroscopy of neoplastic and non neoplastic tissues. Neoplasia **2**, 89–117 (2000)
123. R. Drezek, C. Brookner, I. Pavlova, I. Boiko, A. Malpica, R. Lotan, M. Follen, R. Richards-Kortum, Autofluorescence microscopy of fresh cervical-tissue sections reveals alterations in tissue biochemistry with dysplasia. Photochem. Photobiol. **73**, 636–641 (2001)
124. I. Georgakoudi, B.C. Jacobson, M.G. Muller, E.E. Sheets, K. Badizadegan, D.L. Carr-Locke, C.P. Crum, C.W. Boone, R.R. Dasari, J. Van Dam et al., NAD(P)H and collagen as in vivo quantitative fluorescent biomarkers of epithelial precancerous changes. Cancer Res. **62**, 682–687 (2002)
125. R. Drezek, K. Sokolov, U. Utzinger, I. Boiko, A. Malpica, M. Follen, R. Richards-Kortum, Understanding the contributions of NADH and collagen to cervical tissue fluorescence spectra: modeling, measurements, and implications. J. Biomed. Opt. **6**, 385–396 (2001)
126. A. Zuluaga, U. Utzinger, A. Durkin, H. Fuchs, A. Gillenwater, R. Jacob, B. Kemp, J. Fan, R. Richards-Kortum, Fluorescence excitation emission matrices of human tissue: a system for in vivo measurement and data analysis. Appl. Spectr. **53**, 302–311 (1998)

127. R.A. Zangaro, L. Silveira, R. Manoharan, G. Zonios, I. Itzkan, R. Dasari, J. Van Dam, M.S. Feld, Rapid multiexcitation fluorescence spectroscopy system for in vivo tissue diagnosis. Appl. Opt. **35**, 5211–5219 (1997)
128. N. Ramanujam, M. Follen Mitchell, A. Mahadevan-Jansen, S.L. Thomsen, G. Staerkel, A. Malpica, T. Wright, N. Atkinson, R. Richards-Kortum, Cervical pre-cancer detection using a multivariate statistical algorithm based on laser induced fluorescence spectra at multiple excitation wavelengths. Photochem. Photobiol. **6**, 720–735 (1996)
129. H. Zeng, C. MacAulay, D.I. McLean, B. Palcic, Reconstruction of in vivo skin autofluorescence spectrum from microscopic properties by Monte Carlo simulation. J. Photochem. Photobiol. **38**, 234–240 (1997)
130. D.E. Hyde, T.J. Farrel, M.S. Patterons, B.C. Wilson, A diffusion theory model of spatially resolved fluorescence from depth dependent fluorophore concentrations. Phys. Med. Biol. **46**, 369–383 (2001)
131. Q. Zhang, M. Muller, J. Wu, M.S. Feld, Turbidity free fluorescence spectroscopy of biological tissue. Opt. Lett. **25**, 1451–1453 (2000)
132. F. Koenig, F.J. McGovern, H. Enquist, R. Larne, T.F. Deutsch, K.T. Schomacker, Autofluorescence guided biopsy for the early diagnosis of bladder carcinoma. J. Urol. **159**, 1871–1875 (1998)
133. S. Andersson-Engels, C. Klinteberg, K. Svanberg, S. Svanberg, In vivo fluorescence imaging for tissue diagnostics. Phys. Med. Biol. **42**, 815–824 (1997)
134. N. Stone, C. Kendall, J. Smith, P. Crow, H. Barr, Raman spectroscopy for identification of epithelial cancers. Faraday Discuss. **126**, 141–157 (2004)
135. M. Culha, D. Stokes, T. Vo-Dinh, Surface-enhanced Raman scattering for cancer diagnostics: detection of the BCL2 gene. Expert Rev. Mol. Diagn. **3**(5), 669–675 (2003)
136. T.C. Bakker Schut, M.J. Witjes, H.J. Sterenborg, O.C. Speelman, J.L. Roodenburg, E.T. Marple, H.A. Bruining, G.J. Puppels, In vivo detection of dysplastic tissue by Raman spectroscopy. Anal. Chem. **72**(24), 6010–6018 (2000)
137. N. Stone, P. Stavroulaki, C. Kendall, M. Birchall, H. Barr, Raman spectroscopy for early detection of laryngeal malignancy: preliminary results. Laryngoscope **110**(10 Pt 1), 1756–1763 (2000)
138. A. Mahadevan-Jansen, M.F. Mitchell, N. Ramanujam, A. Malpica, S. Thomsen, U. Utzinger, R. Richards-Kortum, Abstract near-infrared Raman spectroscopy for in vitro detection of cervical precancers. Photochem. Photobiol. **68**(1), 123–132 (1998)
139. L.-P. Choo-Smith, H.G.M. Edwards, H.P. Endtz, J.M. Kros, F. Heule, H. Barr, J.S. Robinson Jr., H.A. Bruining, G.J. Puppels, Medical applications of Raman spectroscopy: from proof of principle to clinical implementation. Biopolymers **67**, 1–9 (2002)
140. M.G. Shim, L.M. Song, N.E. Marcon, B.C. Wilson, In vivo near-infrared Raman spectroscopy: demonstration of feasibility during clinical gastrointestinal endoscopy. Photochem. Photobiol. **72**(1), 146–150 (2000)
141. I.J. Bigio, J.R. Mourant, Ultraviolet and visible spectroscopies for tissue diagnostics: fluorescence spectroscopy and elastic scattering spectroscopy. Phys. Med. Biol. **42**, 803–814 (1997)
142. M.B. Wallace, L.T. Perelman, V. Backman, J.M. Crawford, M. Fitzmaurice, M. Seiler, K. Badizadegan, S.J. Shields, I. Itzkan, R.R. Dasari et al., Endoscopic detection of dysplasia in patients with Barrett's esophagus using light-scattering spectroscopy. Gastroenterology **119**, 677–682 (2000)
143. V. Backman, R. Gurjar, K. Badizadegan, I. Itzkan, R.R. Dasari, L.T. Perelman, M.S. Feld, Polarized light scattering spectroscopy for quantitative measurement of epithelial cellular structures in situ. IEEE J. Sel. Top. Quant. Electron. **5**, 1019–1026 (1999)
144. J.R. Mourant, M. Canpolat, C. Brocker, O. Esponda-Ramos, T.M. Johnson, A. Matanock, K. Stetter, J.P. Freyer, Light scattering from cells: the contribution of the nucleus and the effects of proliferative status. J. Biomed. Opt. **5**, 131–137 (2000)

145. A.L. Clark, A. Gillenwater, R. Alizadeh-Naderi, A.K. El-Naggar, R. Richards-Kortum, Detection and diagnosis of oral neoplasia with an optical coherence microscope. J. Biomed. Opt. **9**(6), 1271–1280 (2004)
146. J.W. Hettinger, M.M. de la Pena, W.R. Myers, M.E. Williams, A. Reeves, R.L. Parsons, R.C. Haskell, R. Wang, J.I. Medford, Optical coherence microscopy. A technology for rapid, in vivo, non-destructive visualization of plants and plant cells. Plant Physiol. **123**, 3–15 (2000)
147. A. Reeves, R.L. Parsons, J.W. Hettinger, J.I. Medford, In vivo three-dimensional imaging of plants with optical coherence microscopy. J. Microsc. **208**, 177–189 (2002)
148. J.A. Izatt, M.D. Kulkarni, H.W. Wang, K. Kobayashi, M.V. Sivak, Optical coherence tomography and microscopy in gastrointestinal tissues and human skin. IEEE J. Sel. Top. Quantum Electron. **2**, 1017–1028 (1996)
149. A.D. Aguirre, P. Hsiung, T.H. Ko, I. Hartl, J.G. Fujimoto, High-resolution optical coherence microscopy for high-speed, in vivo cellular imaging. Opt. Lett. **28**, 2064–2066 (2003)
150. J.A. Izatt, M.R. Hee, G.M. Owen, Optical coherence microscopy in scattering media. Opt. Lett. **19**, 590 (1994)
151. C. Bertrand, P. Corcuff, In vivo spatio-temporal visualization of the human skin by real-time confocal microscopy. Scanning **16**, 150–154 (1993)
152. P. Corcuff, G. Gonnord, G.E. Piérard, J.L. Lévéque, In vivo confocal microscopy of human skin: a new design for cosmetology and dermatology. Scanning **18**, 351–355 (1996)
153. B.R. Masters, D.J. Aziz, A.F. Gmitro, J.H. Kerr, T.C. O'Grady, L. Goldman, Rapid observation of unfixed, unstained human skin biopsy specimens with confocal microscopy and visualization. J. Biomed. Optics **2**, 437–445 (1997)
154. S. González, M. Rajadhyaksha, G. Rubinstein, R.R. Anderson, Characterization of psoriasis in vivo by reflectance confocal microscopy. J. Med. (Westbury) **30**, 337–356 (1999)
155. S. Gonzalez, M. Rajadhyaksha, A. Gonzalez-Serva, W.M. White, R.R. Anderson, Confocal reflectance imaging of folliculitis in vivo: correlation with routine histology. J. Cutaneous Pathol. **26**, 201–205 (1999)
156. K.J. Busam, K. Hester, C. Charles, D.L. Sachs, C.R. Antonescu, S. Gonzalez, A.C. Halpern, Detection of clinically amelanotic malignant melanoma and assessment of its margins by in vivo confocal scanning laser microscopy. Archiv. Dermatol. **137**, 923–929 (2001)
157. R.G. Langley, M. Rajadhyaksha, P.J. Dwyer, A.J. Sober, T.J. Flotte, R.R. Anderson, Confocal scanning laser microscopy of benign and malignant melanocytic skin lesions in vivo. J. Am. Acad. Dermatol. **45**, 365–376 (2001)
158. S. Gonzalez, Z. Tannous, Real-time in vivo confocal reflectance microscopy of basal cell carcinoma. J. Am. Acad. Dermatol. **47**, 869–874 (2002)
159. T. Collier, A. Lacy, R. Richards-Kortum, A. Malpica, M. Follen, Near real-time confocal microscopy of amelanotic tissue: detection of dysplasia in ex vivo cervical tissue. Acad. Radiol. **9**(5), 504–512 (2002)
160. R.A. Drezek, T. Collier, C.K. Brookner, A. Malpica, R. Lotan, R.R. Richards-Kortum, M. Follen, Laser scanning confocal microscopy of cervical tissue before and after application of acetic acid. Am. J. Obstet. Gynecol. **182**, 1135–1139 (2000)
161. H. Inoue, T. Igari, T. Nishikage, K. Ami, T. Yoshida, T. Iwai, A novel method of virtual histopathology using laser-scanning confocal microscopy in-vitro with untreated fresh specimens from the gastrointestinal mucosa. Endoscopy **32**, 439–443 (2000)
162. W.M. White, M. Rajadhyaksha, S. Gonzalez, R.L. Fabian, R.R. Anderson, Noninvasive imaging of human oral mucosa in vivo by confocal reflectance microscopy. Laryngoscope **109**, 1709–1717 (1999)
163. A.M. Clark, A.M. Gillenwater, T.G. Collier, R. Alizadeh-Naderi, A.K. El-Naggar, R. Richards-Kortum, Confocal microscopy for real-time detection of oral cavity neoplasia. Clin. Cancer Res. **9**, 4714–4721 (2003)

164. P. Wilder-Smith, T. Krasieva, W.G. Jung, J. Zhang, Z.P. Chen, K. Osann, B. Tromberg, Non-invasive imaging of oral premalignancy and malignancy. Invited contribution to special edition. J. Biomed. Optics **10**(5), 050601-1-8 (2005)
165. P. Wilder-Smith, W.G. Jung, M. Brenner, K. Osann, H. Beydoun, D. Messadi, Z. Chen, Optical coherence tomography for the diagnosis of oral malignancy. Lasers Surg. Med. **35**, 269–275 (2004)
166. P. Wilder-Smith, K. Lee, S. Guo, J. Zhang, K. Osann, Z. Chen, D. Messadi, In vivo diagnosis of oral dysplasia and malignancy using optical coherence tomography: preliminary studies in 50 patients. Lasers Surg. Med. **41**(5), 353–357 (2009)
167. Z. Hamdoon, W. Jerjes, R. Al-Delayme, G. McKenzie, A. Jay, C. Hopper, Structural validation of oral mucosal tissue using optical coherence tomography. Head Neck Oncol. **4**, 29 (2012). doi:10.1186/1758-3284-4-29